Abstracta

Ano XXIII - N. 05

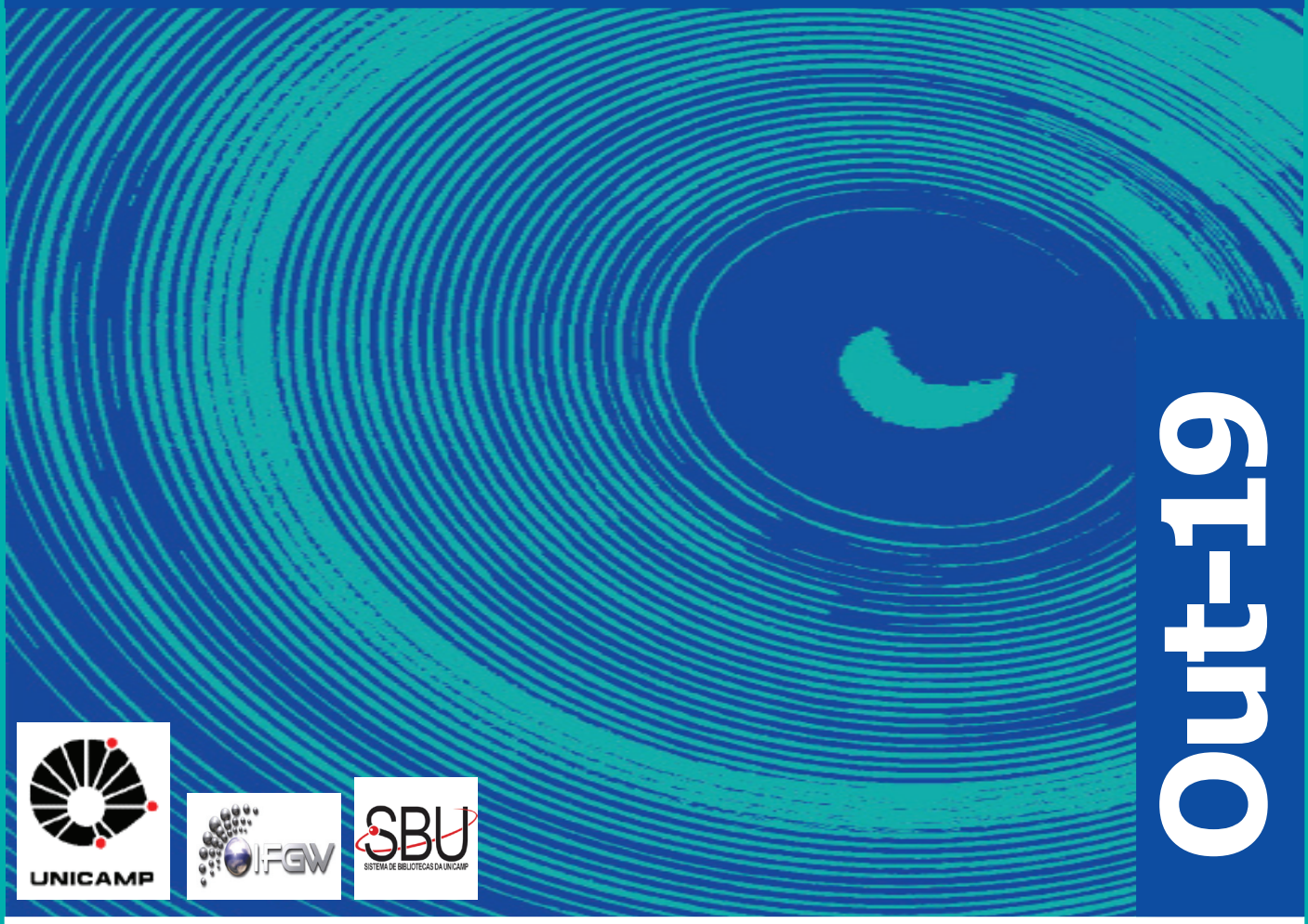

Out-19

Artigos publicados - P298-2019 à P374-2019

Eventos publicados - P375-2019 à P378-2019

Artigos Aceitos para publicação - A002-2019 à A003-2019

Defesas de Teses do IFGW - T008-2019 à T014-2019

Defesas de Dissertações do IFGW - D016-2019 à D021-2019

Artigos publicados

[P298-2019] "A Luminescent Thermometer Exhibiting Slow Relaxation of the Magnetization: Toward Self-Monitored Building Blocks for Next-Generation Optomagnetic Devices"

Errulat, D.; Marin, R.; Galico, D. A.; Harriman, K. L. M.; Pialat, A.; Gabidullin, B.; **Iikawa, F.*; Couto, O. D. D., Jr.***; Moilanen, J. O.; Hemmer, E.; Sigoli, F. A.; Murugesu, M.

The development and integration of Single-Molecule Magnets (SMMs) into molecular electronic devices continue to be an exciting challenge. In such potential devices, heat generation due to the electric current is a critical issue that has to be considered upon device fabrication. To read out accurately the temperature at the submicrometer spatial range, new multifunctional SMMs need to be developed. Herein, we present the first self-calibrated molecular thermometer with SMM properties, which provides an elegant avenue to address these issues. The employment of 2,2'-bipyrimidine and 1,1,1-trifluoroacetylacetonate ligands results in a dinuclear compound, [Dy-2(bpm)(tfaa)(6)], which exhibits slow relaxation of the magnetization along with remarkable photoluminescent properties. This combination allows the gaining of fundamental insight in the electronic properties of the compound and investigation of optomagnetic cross-effects (Zeeman effect). Importantly, spectral variations stemming from two distinct thermal-dependent mechanisms taking place at the molecular level are used to perform luminescence thermometry over the 5-398 K temperature range. Overall, these properties make the proposed system a unique molecular luminescent thermometer bearing SMM properties, which preserves its temperature self-monitoring capability even under applied magnetic fields.

ACS CENTRAL SCIENCE 5[7], 1187-1198, 2019. DOI: 10.1021/acscentsci.9b00288

[P299-2019] "A new RASS galaxy cluster catalogue with low contamination extending to z similar to 1 in the DES overlap region"

Klein, M.; Grandis, S.; Mohr, J. J.; **Sobreira, F.***; et. al.; DES Collaboration

We present the MARD-Y3 catalogue of between 1086 and 2171 galaxy clusters (52 per cent and 65 per cent new) produced using multicomponent matched filter (MCMF) follow-up in 5000 deg(2) of DES-Y3 optical data of the similar to 20 000 overlapping ROSAT All-Sky Survey source catalogue (2RXS) X-ray sources. Optical counterparts are identified as peaks in galaxy richness as a function of redshift along the line of sight towards each 2RXS source within a search region informed by an X-ray prior. All peaks are assigned a probability f(cont) of being a random superposition. The clusters lie at $0.02 < z < 1.1$ with more than 100 clusters at $z > 0.5$. Residual contamination is 2.6 per cent and 9.6 per cent for the cuts adopted here. For each cluster we present the optical centre, redshift, rest frame X-ray luminosity, M-500 mass, coincidence with NWAY infrared sources, and estimators of dynamical state. About 2 per cent of MARD-Y3 clusters have multiple possible counterparts, the photo-z's are high quality with sigma(Delta z/(1 + z)) = 0.0046, and similar to 1 per cent of clusters exhibit evidence of X-ray luminosity boosting from emission by cluster active galactic nuclei. Comparison with other catalogues (MCXC, RM, SPT-SZ, Planck) is performed to test consistency of richness, luminosity, and mass estimates. We measure the MARD-Y3 X-ray luminosity function and compare it to the expectation from a fiducial cosmology and externally calibrated luminosity-and richness--mass relations. Agreement is good, providing evidence that MARD-Y3 has low contamination and can be understood as a simple two step selection - X-ray and then optical - of an underlying cluster population described by the halo mass function.

MONTHLY NOTICES OF THE ROYAL ASTRONOMICAL SOCIETY 488[1], 739-769, 2019. DOI: 10.1093/mnras/stz1463

[P300-2019] "A New Standard DNA Damage (SDD) Data Format"

Schuemann, J.; McNamara, A. L.; Warmenhoven, J. W.; **Bernal, M. A.***; et. al.

Our understanding of radiation-induced cellular damage has greatly improved over the past few decades. Despite this progress, there are still many obstacles to fully understand how radiation interacts with biologically relevant cellular components, such as DNA, to cause observable end points such as cell killing. Damage in DNA is identified as a major route of cell killing. One hurdle when modeling biological effects is the difficulty in directly comparing results generated by members of different research groups. Multiple Monte Carlo codes have been developed to simulate damage induction at the DNA scale, while at the same time various groups have developed models that describe DNA repair processes with varying levels of detail. These repair models are intrinsically linked to the damage model employed in their development, making it difficult to disentangle systematic effects in either part of the modeling chain. These modeling chains typically consist of track-structure Monte Carlo simulations of the physical interactions creating direct damages to DNA, followed by simulations of the production and initial reactions of chemical species causing so-called ''indirect'' damages. After the induction of DNA damage, DNA repair models combine the simulated damage patterns with biological models to determine the biological consequences of the damage. To date, the effect of the environment, such as molecular oxygen (normoxic vs. hypoxic), has been poorly considered. We propose a new standard DNA damage (SDD) data format to unify the interface between the simulation of damage induction in DNA and the biological modeling of DNA repair processes, and introduce the effect of the environment (molecular oxygen or other compounds) as a flexible parameter. Such a standard greatly facilitates inter-model comparisons, providing an ideal environment to tease out model assumptions and identify persistent, underlying mechanisms. Through inter-model comparisons, this unified standard has the potential to greatly advance our understanding of the underlying mechanisms of radiation-induced DNA damage and the resulting observable biological effects when radiation parameters and/or environmental conditions change.

RADIATION RESEARCH 191[1], 76-92, 2019. DOI: 10.1667/RR15209.1

[P301-2019] "A search for pair production of new light bosons decaying into muons in proton-proton collisions at 13 TeV"

Sirunyan, A. M.; Tumasyan, A.; Adam, W.; **Chinellato, J. A.*; Tonelli Manganote, E. J.***; et. al.; CMS Collaboration

A search for new light bosons decaying into muon pairs is presented using a data sample corresponding to an integrated luminosity of 35.9 fb(-1) of proton-proton collisions at a center-of-mass energy root s = 13 TeV, collected with the CMS detector at the CERN LHC. The search is model independent, only requiring the pair production of a new light boson and its subsequent decay to a pair of muons. No significant deviation from the predicted background is observed. A model independent limit is set on the product of the production cross section times branching fraction to dimuons squared times acceptance as a function of new light boson mass. This limit varies between 0.15 and 0.39 fb over a range of new light boson masses from 0.25 to 8.5 GeV. It is then interpreted in the context of the next-to-minimal supersymmetric standard model and a dark supersymmetry model that allows for nonnegligible light boson lifetimes.

In both cases, there is significant improvement over previously published limits.

PHYSICS LETTERS B 796, 131-154, 2019. DOI: 10.1016/j.physletb.2019.07.013

[P302-2019] "An Extended Catalog of Galaxy-Galaxy Strong Gravitational Lenses Discovered in DES Using Convolutional Neural Networks"

Jacobs, C.; Collett, T.; Glazebrook, K.; **Sobreira, F.***; et. al.; DES Collaboration

We search Dark Energy Survey (DES) Year 3 imaging for galaxy--galaxy strong gravitational lenses using convolutional neural networks, extending previous work with new training sets and covering a wider range of redshifts and colors. We train two neural networks using images of simulated lenses, then use them to score postage-stamp images of 7.9 million sources from DES chosen to have plausible lens colors based on simulations. We examine 1175 of the highest-scored candidates and identify 152 probable or definite lenses. Examining an additional 20,000 images with lower scores, we identify a further 247 probable or definite candidates. After including 86 candidates discovered in earlier searches using neural networks and 26 candidates discovered through visual inspection of blue-near-red objects in the DES catalog, we present a catalog of 511 lens candidates.

ASTROPHYSICAL JOURNAL SUPPLEMENT SERIES 243[1], 17, 2019. DOI: 10.3847/1538-4365/ab26b6

[P303-2019] "Biomechanical behaviour of bulk-fill resin composites in class II restorations"

Lins, R. B. E.; **Aristilde, S.*; Osorio, J. H.*; Cordeiro, C. M. B.***; Yanikian, C. R. F.; Bicalho, A. A.; Stape, T. H. S.; Soares, C. J.; Martins, L. R. M.

The aim of this study was to evaluate the biomechanical properties expressed by shrinkage stress, cuspal strain, fracture strength and failure mode in molars with large class II mesio-occlusal-distal restorations. Sixty-four human caries--free third molars were selected and distributed randomly into four groups: Z100 restorative material (Z100), Tetric N--Ceram Bulk-Fill (TNC), Filtek Bulk-Fill (FBF) and Aura Ultra Universal (ABF). The bulk-fill materials were inserted in one singular bulk increment and the conventional composite resin in three ones. Polymerisation shrinkage stress was evaluated by optical Fibre Bragg Gratings (FBG) sensors (n = 6). The cuspal deformation was measured using an extensometer during three moments: restorative procedure, axial compressive loading and at fracture (n = 10). The fracture strength was evaluated on a universal machine. The failure mode was analysed by Scanning Electron Microscopy (SEM). Data were analysed using one-way ANOVA tests with Tukey's posthoc test (alpha = 5%). Data of the failure mode were submitted to a likelihood ratio chi-square test. Z100 presented the highest mean value for the shrinkage stress ($p < 0.05$) by FBG evaluation, whereas bulk-fill resin groups presented low polymerisation stress mean value, especially the TNC ($p < 0.05$). The cuspal deformation test showed that Z100 presented a significant difference mean value compared to the other groups ($p < 0.01$) during the restoration and compressive axial force; however, load until the fracture presented a difference only between TNC and FBF ($p < 0.05$). The fracture strength of TNC was statistically different from Z100 ($p < 0.01$). The failure mode was not statistically different in all the groups ($p > 0.05$). Bulk-fill composites promoted less polymerisation shrinkage stress than conventional microhybrid composite during and after the light curing process in class II posterior resin composite restorations.

JOURNAL OF THE MECHANICAL BEHAVIOR OF BIOMEDICAL MATERIALS 98, 255-261, 2019.

DOI: 10.1016/j.jmbbm.2019.06.032

[P304-2019] "Brillouin optomechanics in nanophotonic structures"

Wiederhecker, G. S.*; Dainese, P.*; Alegre, T. P. M.*

The interaction between light and mesoscopic mechanical degrees of freedom has been investigated under various perspectives, from spectroscopy in condensed matter, optical tweezer particle trapping, and long-haul optical fiber communication system penalties to gravitational-wave detector noise. In the context of integrated photonics, two topics with dissimilar origins-cavity optomechanics and guided wave Brillouin scattering-are rooted in the manipulation and control of the energy exchange between trapped light and mechanical modes. In this tutorial, we explore the impact of optical and mechanical subwavelength confinement on the interaction among these waves, coined as Brillouin optomechanics. At this spatial scale, optical and mechanical fields are fully vectorial and the common intuition that more intense fields lead to stronger interaction may fail. Here, we provide a thorough discussion on how the two major physical effects responsible for the Brillouin interaction-photoelastic and moving-boundary effects-interplay to foster exciting possibilities in this field. In order to stimulate beginners into this growing research field, this tutorial is accompanied by all the discussed simulation material based on a widespread commercial finite-element solver.

APL PHOTONICS 4[7], 071101, 2019. DOI: 10.1063/1.5088169

[P305-2019] "Brillouin optomechanics in nanophotonic structures"

Wiederhecker, G. S.*; Dainese, P.*; Alegre, T. P. M.*

The interaction between light and mesoscopic mechanical degrees of freedom has been investigated under various perspectives, from spectroscopy in condensed matter, optical tweezer particle trapping, and long-haul optical fiber communication system penalties to gravitational-wave detector noise. In the context of integrated photonics, two topics with dissimilar origins-cavity optomechanics and guided wave Brillouin scattering-are rooted in the manipulation and control of the energy exchange between trapped light and mechanical modes. In this tutorial, we explore the impact of optical and mechanical subwavelength confinement on the interaction among these waves, coined as Brillouin optomechanics. At this spatial scale, optical and mechanical fields are fully vectorial and the common intuition that more intense fields lead to stronger interaction may fail. Here, we provide a thorough discussion on how the two major physical effects responsible for the Brillouin interaction-photoelastic and moving-boundary effects-interplay to foster exciting possibilities in this field. In order to stimulate beginners into this growing research field, this tutorial is accompanied by all the discussed simulation material based on a widespread commercial finite-element solver.

APL PHOTONICS 4[7], 071101, 2019. DOI: 10.1063/1.5088169

[P306-2019] "Causality and dissipation in relativistic polarizable fluids"

Montenegro, D.*; Torrieri, G.*

Using field theory techniques we analyze the perfect fluid limit, defined as fastest possible local equilibration, in a medium with polarizability, defined as a nonzero local equilibrium partition of angular momentum into spin and vorticity. We show that to restore causality a relaxation term linking vorticity and polarization,

analogous to the Israel-Stewart term linking viscous forces and gradients, is required. This term provides the minimum amount of dissipation a locally thermalized relativistic medium with polarizability must have, independently of its underlying degrees of freedom. For materials susceptible to spin alignment an infrared acausal mode remains, which we interpret as a Banks-Casher mode signaling spontaneous transition to a polarized phase. With these ingredients, we propose a candidate for a fully causal Lagrangian of a relativistic polarizable system near the perfect fluid limit, and close with some phenomenological considerations.

PHYSICAL REVIEW D 100[5], 056011, 2019. DOI: 10.1103/PhysRevD.100.056011

[P307-2019] "CeAu2Bi: A new nonsymmorphic antiferromagnetic compound"

Piva, M. M.*; Zhu, W.; Ronning, F.; Thompson, J. D.; **Pagliuso, P. G.*; Rosa, P. F. S.***

Here, we report the structural and electronic properties of CeAu2Bi, a new heavy-fermion compound crystallizing in a nonsymmorphic hexagonal structure (P63/mmc). The Ce3+ ions form a triangular lattice which orders antiferromagnetically below T-N = 3.1 K with a magnetic hard axis along the c axis. Under applied pressure, T-N increases linearly at a rate of 0.07 K/kbar, indicating that the Ce f electrons are fairly localized. In fact, heat capacity measurements provide an estimate of 150(10) mJ/mol K-2 for the Sommerfeld coefficient. The crystal-field scheme obtained from our thermodynamic data points to a ground state with a dominantly vertical bar j(z) = +/- 1/2 > character, which commonly occurs in systems with a hard c axis. Finally, electronic band structure calculations and symmetry analysis in k space reveal that CeAu2Bi hosts symmetry-protected crossings at k(z) = pi in the paramagnetic state.

PHYSICAL REVIEW MATERIALS 3[7], 071202, 2019. DOI: 10.1103/PhysRevMaterials.3.071202

[P308-2019] "Centrality and pseudorapidity dependence of the transverse energy density in pPb collisions ats root s(NN)=5.02 TeV"

Sirunyan, A. M.; Tumasyan, A.; Adam, W.; **Chinellato, J. A.*; Tonelli Manganote, E. J.***; et. al.; CMS Collaboration

The almost hermetic coverage of the CMS detector is used to measure the distribution of transverse energy, E-T, over 13.2 units of pseudorapidity, eta, for pPb collisions at a center-of-mass energy per nucleon pair of root s(NN) = 5.02 TeV. The huge angular acceptance exploits the fact that the CASTOR calorimeter at -6.6 < eta < -5.2 is effectively present on both sides of the colliding system because of a switch in the proton-going and lead-going beam directions. This wide acceptance enables the study of correlations between well-separated angular regions and makes the measurement a particularly powerful test of event generators. For minimum bias pPb collisions the maximum value of dE(T)/d eta is 22 GeV, which implies an E-T per participant nucleon pair comparable to that of peripheral PbPb collisions at root s(NN) 7 = 2.76 TeV. The increase of dE(T)/d eta with centrality is much stronger for the lead-going side than for the proton-going side. The i dependence of dE(T)/d eta is sensitive to the eta range in which the centrality variable is defined. Several modern generators are compared to these results but none is able to capture all aspects of the eta and centrality dependence of the data and the correlations observed between different eta regions.

PHYSICAL REVIEW C 100[2], 024902, 2019. DOI: 10.1103/PhysRevC.100.024902

[P309-2019] "Characterization of the varying flux of atmospheric muons measured with the Large Volume Detector for 24 years"

Agafonova, N. Yu.; Aglietta, M.; Antonioli, P.; **Kemp, E.***; et. al.; LVD Collaboration

The Large Volume Detector, hosted in the INFN Laboratori Nazionali del Gran Sasso, is triggered by atmospheric muons at a rate of similar to 0.1 Hz. The data collected over almost a quarter of a century are used to study the muon intensity underground. The 5 x 10(7) muon series, the longest ever exploited by an underground instrument, allows for the accurate long-term monitoring of the muon intensity underground. This is relevant as a study of the background in the Gran Sasso Laboratory, which hosts a variety of long-duration, low-background detectors. We describe the procedure to select muon-like events as well as the method used to compute the exposure. We report the value of the average muon flux measured from 1994 to 2017: I-mu(0) = 13.35 +/- 0.0005(stat) +/- 0.03(sys) x 10(-4) m(-2) S-1. We show that the intensity is modulated around this average value due to temperature variations in the stratosphere. We quantify such a correlation by using temperature data from the European Center for Medium-range Weather Forecasts: we find an effective temperature coefficient alpha(T) = 0.94 +/- 0.01(stat) +/- 0.01(sys), in agreement with other measurements at the same depth. We scrutinize the spectral content of the time series of the muon intensity by means of the Lomb-Scargle analysis. This yields the evidence of a 1-year periodicity, as well as the indication of others, both shorter and longer, suggesting that the series is not a pure sinusoidal wave. Consequently, and for the first time, we characterize the observed modulation in terms of amplitude and position of the maximum and minimum on a year-by-year basis.

PHYSICAL REVIEW D 100[6], 062002, 2019. DOI: 10.1103/PhysRevD.100.062002

[P310-2019] "Coevolution Creates Complex Mosaics across Large Landscapes"

Fernandes, L. D.; Lemos-Costa, P.; Guimaraes, P. R., Jr.; Thompson, J. N.; **Aguiar, M. A. M. de***

The spatial distribution of populations can influence the evolutionary outcome of species interactions. The variation in direction and strength of selection across local communities creates geographic selection mosaics that, when combined with gene flow and genomic processes such as genome duplication or hybridization, can fuel ongoing coevolution. A fundamental problem to solve is how coevolution proceeds when many populations that vary in their ecological outcomes are connected across large landscapes. Here we use a lattice model to explore this problem. Our results show that the complex interrelationships among the elements of the geographic mosaic of coevolution can lead to the formation of clusters of populations with similar phenotypes that are larger than expected by local selection. Our results indicate that neither the spatial distribution of phenotypes nor the spatial differences in magnitude and direction of selection alone dictate coevolutionary dynamics: the geographic mosaic of coevolution affects formation of phenotypic clusters, which in turn affect the spatial and temporal dynamics of coevolution. Because the formation of large phenotypic clusters depends on gene flow, we predict that current habitat fragmentation will change the outcomes of geographic mosaics, coupling spatial patterns in selection and phenotypes.

AMERICAN NATURALIST 194[2], 217-229, 2019. DOI: 10.1086/704157

[P311-2019] "Conduction electrons in aperiodic versus periodic structures: An ESR study of quasicrystalline i-Y(Gd)-Cd and its approximant Y(Gd)Cd-6"

Cabrera-Baez, M.*; Avila, M. A.; **Rettori, C.***

A formal description of collective electronic states in condensed-matter systems lacking long-range periodicity remains a theoretical challenge. To experimentally explore the differences in electronic and magnetic behavior between metallic quasicrystals (QCs) and their conventional crystalline analogs [quasicrystal approximants (QCAs)], we have grown single crystals of Y1-xGdx-Cd6 (QCA) together with their QC counterparts i-Y1-xGdx-Cd for x = 0.006, 0.01, 0.1, and 1.00, and we carried out comparative T-dependent electron spin resonance (ESR) measurements. On the high Gd concentration side, x = 1.00, we confirm that GdCd6 adopts an antiferromagnetic ground state below T-N similar to 22 K, whereas i--Gd-Cd presents spin-glass-like behavior showing similar local and dynamical properties from the point of view of ESR. For the diluted samples, our ESR experimental results show similar local conduction electron polarization behavior at the Gd3+ site in all QC/QCA pairs investigated, supporting the validity of using QCAs as periodic representations of QCs in terms of short-range electronic interactions. However, there is a measurable difference in the Korringa relaxation rate (spin-flip relaxation process between the localized Gd3+ 4f electron and the delocalized s-type conduction electrons at the Fermi surface) between the QC/QCA pairs probably associated with the lack of periodicity. We expect that our comparative ESR study may provide support and motivation for the development of new theoretical approaches toward a generalized band-structure theory, contemplating condensed--matter systems beyond the scope of traditional periodicity.

PHYSICAL REVIEW B 100[1], 014207, 2019. DOI: 10.1103/PhysRevB.100.014207

[P312-2019] "Constraints on the redshift evolution of astrophysical feedback with Sunyaev-Zel'dovich effect cross--correlations"

Pandey, S.; Baxter, E. J.; Xu, Z.; **Sobreira, F.***; et. al.;

An understanding of astrophysical feedback is important for constraining models of galaxy formation and for extracting cosmological information from current and future weak lensing surveys. The thermal Sunyaev-Zel'dovich effect, quantified via the Compton-y parameter, is a powerful tool for studying feedback, because it directly probes the pressure of the hot, ionized gas residing in dark matter halos. Cross-correlations between galaxies and maps of Compton-y obtained from cosmic microwave background surveys are sensitive to the redshift evolution of the gas pressure, and its dependence on halo mass. In this work, we use galaxies identified in year one data from the Dark Energy Survey and Compton-y maps constructed from Planck observations. We find highly significant (roughly 12 sigma) detections of galaxy-y cross--correlation in multiple redshift bins. By jointly fitting these measurements as well as measurements of galaxy clustering, we constrain the halo bias-weighted, gas pressure of the Universe as a function of redshift between 0.15 less than or similar to z less than or similar to 0.75. We compare these measurements to predictions from hydrodynamical simulations, allowing us to constrain the amount of thermal energy in the halo gas relative to that resulting from gravitational collapse.

PHYSICAL REVIEW D 100[6], 063519, 2019. DOI: 10.1103/PhysRevD.100.063519

[P313-2019] "Crystalline electric field study in a putative topologically trivial rare-earth doped YPdBi compound"

Souza, J. C.*; Jesus, C. B. R.*; Lesseux, G. G.*; Rosa, P. F. S.*; Urbano, R. R.*; Pagliuso, P. G.*

Topological states of matter have attracted a lot of attention recently due to their intriguing physical properties and potential applications. In particular, the family of half-Heusler compounds RMT (R = rare earth, M = Pt, Pd or Au, and T. Bi, Sb, Pb or Sn) has been predicted to display tunable topological properties via their cubic unit cell volume and/or the charges of the M and T atoms. In this work, we report electron spin resonance (ESR), along with complementary macroscopic experiments, in the putative topologically trivial rare-earth doped (Gd, Nd and Er) YPdBi. From magnetic susceptibility data analysis constrained by ESR results, we were able to extract the fourth (A(4)) and sixth (A(6)) order crystal field parameters (CFP) for YPdBi and compared them with those already reported to YPtBi, which is known as a topologically non-trivial compound. We observed that the sign of the CFP changes systematically from YPdBi to YPtBi, possibly due to the inversion of the valence and conduction bands at the Fermi level. The enhanced spin-orbit coupling in YPtBi, when compared to YPdBi, induces the band inversion that drives the system to a non-trivial topological state. This band inversion likely has an effect on the effective charges surrounding the magnetic dopants that are probed by the CFP.

JOURNAL OF PHYSICS-CONDENSED MATTER 31[46], 465701, 2019. DOI: 10.1088/1361-648X/ab33e9

[P314-2019] "Dark Energy Survey Year 1 Results: Cross--correlation between Dark Energy Survey Y1 galaxy weak lensing and South Pole Telescope plus Planck CMB weak lensing"

Omori, Y.; Baxter, E. J.; Chang, C.; **Sobreira, F.***; et. al.; DES Collaboration; SPT Collaboration

We cross-correlate galaxy weak lensing measurements from the Dark Energy Survey (DES) year-one data with a cosmic microwave background (CMB) weak lensing map derived from South Pole Telescope (SPT) and Planck data, with an effective overlapping area of 1289 deg(2). With the combined measurements from four source galaxy redshift bins, we obtain a detection significance of 5.8 sigma. We fit the amplitude of the correlation functions while fixing the cosmological parameters to a fiducial Lambda CDM model, finding A = 0.99 +/- 0.17. We additionally use the correlation function measurements to constrain shear calibration bias, obtaining constraints that are consistent with previous DES analyses. Finally, when performing a cosmological analysis under the Lambda CDM model, we obtain the marginalized constraints of Omega(m) = 0.261(-0.051)(+0.070) and S-8 = sigma(8)root Omega(m)/0.3 = 0.660(-0.100)(+0.085). These measurements are used in a companion work that presents cosmological constraints from the joint analysis of two-point functions among galaxies, galaxy shears, and CMB lensing using DES, SPT, and Planck data.

PHYSICAL REVIEW D 10[4], 043517, 2019. DOI: 10.1103/PhysRevD.100.043517

[P315-2019] "Dark Energy Survey year 1 results: Joint analysis of galaxy clustering, galaxy lensing, and CMB lensing two-point functions"

Abbott, T. M. C.; Abdalla, F. B.; Alarcon, A.; **Sobreira, F.***; et. al.; DES Collaboration; SPT Collaboration

We perform a joint analysis of the auto and cross-correlations between three cosmic fields: the galaxy density field, the galaxy weak lensing shear field, and the cosmic microwave background (CMB) weak lensing convergence field. These three fields are measured using roughly 1300 sq. deg. of overlapping optical imaging data from first year observations of the Dark Energy Survey (DES) and millimeter-wave observations of the CMB from both the South Pole Telescope Sunyaev-Zel'dovich survey and Planck.

We present cosmological constraints from the joint analysis of the two-point correlation functions between galaxy density and galaxy shear with CMB lensing. We test for consistency between these measurements and the DES-only two-point function measurements, finding no evidence for inconsistency in the context of flat Lambda CDM cosmological models. Performing a joint analysis of five of the possible correlation functions between these fields (excluding only the CMB lensing autospectrum) yields S-8 sigma(8) root Omega(m)/0.3 = 0.782(-0.025)(+0.019) and Omega(m) = 0.260(-0.019)(+0.029). We test for consistency between these five correlation function measurements and the Planck-only measurement of the CMB lensing autospectrum, again finding no evidence for inconsistency in the context of flat Lambda CDM models. Combining constraints from all six two-point functions yields S-8 = 0.776(-0.021)(+0.014) and Omega(m) = 0.271(-0.016)(+0.022). These results provide a powerful test and confirmation of the results from the first year DES joint-probes analysis.

PHYSICAL REVIEW D 100[2], 023541, 2019. DOI: 10.1103/PhysRevD.100.023541

[P316-2019] "Dark Energy Survey Year 1 results: measurement of the galaxy angular power spectrum"

Camacho, H.; Kokron, N.; Andrade-Oliveira, F.; **Sobreira, F.***; e. al.; DES Collaboration

We use data from the first-year observations of the DES collaboration to measure the galaxy angular power spectrum (APS), and search for its BAO feature. We test our methodology in a sample of 1800 DES Y1-like mock catalogues. We use the pseudo-C-l, method to estimate the APS and the mock catalogues to estimate its covariance matrix. We use templates to model the measured spectra and estimate template parameters firstly from the G's of the mocks using two different methods, a maximum likelihood estimator and a Markov Chain Monte Carlo, finding consistent results with a good reduced chi(2). Robustness tests are performed to estimate the impact of different choices of settings used in our analysis. Finally, we apply our method to a galaxy sample constructed from DES Y1 data specifically for LSS studies. This catalogue comprises galaxies within an effective area of 1318 deg(2) and 0.6 < z < 1.0. We find that the DES Y1 data favour a model with BAO at the 2.6 sigma C.L. However, the goodness of fit is somewhat poor, with chi(2)/(d.o.f.) = 1.49. We identify a possible cause showing that using a theoretical covariance matrix obtained from C-l's that are better adjusted to data results in an improved value of chi(2)/(dof) = 1.36 which is similar to the value obtained with the real-space analysis. Our results correspond to a distance measurement of D-A (Z(eff) = 0.81)/r(d) = 10.65 +/- 0.49, consistent with the main DES BAO findings. This is a companion paper to the main DES BAO article showing the details of the harmonic space analysis.

MONTHLY NOTICES OF THE ROYAL ASTRONOMICAL SOCIETY 487[3], 3870-3883, 2019. DOI: 10.1093/mnras/stz1514

[P317-2019] "Dark Energy Survey Year 1 results: the effect of intracluster light on photometric redshifts for weak gravitational lensing"

Gruen, D.; Zhang, Y.; Palmese, A.; **Sobreira, F.***; et. al.; DES Collaboration

We study the effect of diffuse intracluster light on the critical surface mass density estimated from photometric redshifts of lensing source galaxies, and the resulting bias in a weak lensing measurement of galaxy cluster mass. Under conservative assumptions, we find the bias to he negligible for imaging surveys like the Dark Energy Survey with a recommended scale cut of >= 200 kpc distance from cluster centres. For significantly deeper lensing source galaxy catalogues from present and future surveys like the Large Synoptic Survey Telescope program, more conservative scale and source magnitude cuts or a correction of the effect may be necessary to achieve percent level lensing measurement accuracy, especially at the massive end of the cluster population.

MONTHLY NOTICES OF THE ROYAL ASTRONOMICAL SOCIETY 488[3], 4389-4399, 2019. DOI: 10.1093/mnras/stz2036

[P318-2019] "Dark Energy Survey Year 1 Results: Tomographic cross-correlations between Dark Energy Survey galaxies and CMB lensing from South Pole Telescope plus Planck"

Omori, Y.; Giannantonio, T.; Porredon, A.; **Sobreira, F.***; et. al.; DES Collaboration; SPT Collaboration

We measure the cross-correlation between REDMAGIC galaxies selected from the Dark Energy Survey (DES) year 1 data and gravitational lensing of the cosmic microwave background (CMB) reconstructed from South Pole Telescope (SPT) and Planck data over 1289 deg(2). When combining measurements across multiple galaxy redshift bins spanning the redshift range of 0.15 < z < 0.90, we reject the hypothesis of no correlation at 19.9 sigma significance. When removing small-scale data points where thermal Sunyaev-Zel'dovich signal and nonlinear galaxy bias could potentially bias our results, the detection significance is reduced to 9.9 sigma. We perform a joint analysis of galaxy-CMB lensing cross-correlations and galaxy clustering to constrain cosmology, finding Omega m = 0.276(-0.030)(+0.029) and S-8 = sigma(8) root Omega(m)/0.3 = 0.800(-0.094)(+0.090). we also perform two alternate analyses aimed at constraining only the growth rate of cosmic structure as a function of redshift, finding consistency with predictions from the concordance Lambda CDM model. The measurements presented here are part of a joint cosmological analysis that combines galaxy clustering, galaxy lensing and CMB lensing using data from DES, SPT and Planck.

PHYSICAL REVIEW D 100[4], 043501, 2019. DOI: 10.1103/PhysRevD.100.043501

[P319-2019] "Detecting the macroevolutionary signal of species interactions"

Harmon, L. J.; Andreazzi, C. S.; Debarre, F.; Drury, J.; Goldberg, E. E.; **Martins, A. B.***; Melian, C. J.; Narwani, A.; Nuismer, S. L.; Pennell, M. W.; Rudman, S. M.; Seehausen, O.; Silvestro, D.; Weber, M.; Matthews, B.

Species interactions lie at the heart of many theories of macroevolution, from adaptive radiation to the Red Queen. Although some theories describe the imprint that interactions will have over long timescales, we are still missing a comprehensive understanding of the effects of interactions on macroevolution. Current research shows strong evidence for the impact of interactions on macroevolutionary patterns of trait evolution and diversification, yet many macroevolutionary studies have only a tenuous relationship to ecological studies of interactions over shorter timescales. We review current research in this area, highlighting approaches that explicitly model species interactions and connect them to broad-scale macroevolutionary patterns. We also suggest that progress has been made by taking an integrative interdisciplinary look at individual clades. We focus on African cichlids as a case study of how this approach can be fruitful. Overall, although the evidence for species interactions shaping macroevolution is strong, further work using integrative and model-based approaches is needed to spur progress towards understanding the complex dynamics that structure communities over time and space.

JOURNAL OF EVOLUTIONARY BIOLOGY 32[8], 769-782, 2019. DOI: 10.1111/jeb.13477

[P320-2019] "Energy extraction of a chaotic system in a cyclic process: a Szilard engine perspective"

Soriani, A.*; Bonanca, M. V. S.*

Inspired by the available examples of microcanonical Szilard engines and by the original Szilard engine, we devise a system with two degrees of freedom whose ensemble average energy, starting with a microcanical ensemble, decreases after a cyclic variation of its external parameters. We use the ergodic adiabatic theorem to motivate our cycle and numerical simulations to check the decrement in the average energy. We then compare our system to the aforementioned Szilard engines, microcanonical or not, and speculate about symmetry breaking being the cause of energy extraction in cyclic processes, even when non-integrability and chaos are present.

JOURNAL OF STATISTICAL MECHANICS-THEORY AND EXPERIMENT 083210, 2019. DOI: 10.1088/1742-5468/ab345a

[P321-2019] "Evidence of precursor orthorhombic domains well above the electronic nematic transition temperature in Sr(Fe1-xCox)(2)As-2"

Kaneko, U. F.; **Piva, M. M.*; Jesus, C. B. R.*; Saleta, M. E.*; Urbano, R. R.*; Pagliuso, P. G.*; Granado, E.***

Raman scattering, synchrotron x-ray diffraction, specific heat, resistivity and magnetic susceptibility measurements were performed in Sr(Fe1-xCox)(2)As-2[x = 0.20(3)] single crystals with superconducting critical temperature T-c = 22 K and two additional transitions at 132 and 152 K observed in both specific heat and resistivity data. A quasielastic Raman signal with B-2g symmetry (tetragonal cell) associated with electronic nematic fluctuations is observed. Crucially, this signal shows maximum intensity at T-o similar to 132 K, marking the nematic transition temperature. X-ray diffraction shows evidence of coexisting orthorhombic and tetragonal domains between T-nem and T-nem similar to 152 K, implying that precursor orthorhombic domains emerge over an extended temperature range above T-nem. While the height of the quasielastic Raman peak is insensitive to T-o, the temperature-dependence of the average nematic fluctuation rate indicates a slowing down of the nematic fluctuations inside the precursor orthorhombic domains. These results are analogous to those previously reported for the LaFeAsO parent oxypnictide (Kaneko et al 2017 Phys. Rev. B 96 014506). We propose a scenario where the precursor orthorhombic phase may be generated within the electronically disordered regime (T > T-nem) as long as the nematic fluctuation rate is sufficiently small in comparison to the optical phonon frequency range. In this regime, the local atomic structure responds adiabatically to the electronic nematic fluctuations, creating a net of orthorhombic clusters that, albeit dynamical for T > T-nem, may be sufficiently dense to sustain long-range phase coherence in a diffraction process up to T-o.

JOURNAL OF PHYSICS-CONDENSED MATTER 31[49], 495402, 2019. DOI: 10.1088/1361-648X/ab2ffc

[P322-2019] "Exploring the synthesis conditions to control the morphology of gold-iron oxide heterostructures"

Tancredi, P.; da Costa, L. S.; Calderon, S.; **Moscoso-Londono, O.***; Socolovsky, L. M.; Ferreira, P. J.; **Muraca, D.***; Zanchet, D.; **Knobel, M.***

Gold-iron oxide nano-heterostructures with a clear and well-defined morphology were prepared via a seed-assisted method. The synthesis process and the events of heterogeneous nucleation during the decomposition of the iron precursor were carefully studied in order to understand the mechanism of the reaction and to tailor the architecture of the fabricated heterostructures. When employing Au seeds of 3 and 5 nm, nanoparticles with a dimer-like morphology were produced due to the occurrence of a single iron oxide nucleation event. Otherwise, multi-nucleation events could be favored by two mechanisms: (i) by the incorporation of a reducing agent and the slowing down of the heating protocol, leading to a core-shell system; (ii) by the increase of the Au seed size to 8 nm, leading to a flower-like system. Further increase of the Au seed size to 12 nm using similar synthesis conditions promotes the homogeneous nucleation and growth of the iron oxide phase, without formation of heterostructures. An in-depth study was performed on the gold-iron oxide heterostructures to confirm the epitaxial growth of the oxide domain over the Au seed and to analyze the elemental distribution of the components within the heterostructures. Finally, it was found that the modification of the plasmonic properties of the Au nanoparticles are strongly influenced by the architecture of the heterostructure, with a more pronounced damping effect for the systems produced after multi-nucleation events.

NANO RESEARCH 12[8], 1781-1788, 2019. DOI: 10.1007/s12274-019-2431-7

[P323-2019] "First Observation of an Attractive Interaction between a Proton and a Cascade Baryon"

Acharya, S.; Adamova, D.; Adhya, S. P.; **Albuquerque, D. S. D.*; Chinellato, D. D.*; De Souza, R. D.*; Takahashi, J.***; et. al.; A Large Ion Collider Expt Collabor

This Letter presents the first experimental observation of the attractive strong interaction between a proton and a multistrange baryon (hyperon) Xi(-). The result is extracted from two-particle correlations of combined p-Xi(-) circle plus (p) over bar-(Xi) over bar (+) pairs measured in p-Pb collisions at root S-NN = 5.02 TeV at the LHC with ALICE. The measured correlation function is compared with the prediction obtained assuming only an attractive Coulomb interaction and a standard deviation in the range [3.6, 5.3] is found. Since the measured p-Xi(-)circle plus(p) over bar-(Xi) over bar (+) correlation is significantly enhanced with respect to the Coulomb prediction, the presence of an additional, strong, attractive interaction is evident. The data are compatible with recent lattice calculations by the HAL-QCD Collaboration, with a standard deviation in the range [1.8, 3.7]. The lattice potential predicts a shallow repulsive Xi(-). interaction within pure neutron matter and this implies stiffer equations of state for neutron-rich matter including hyperons. Implications of the strong interaction for the modeling of neutron stars are discussed.

PHYSICAL REVIEW LETTERS 123[11], 112002, 2019. DOI: 10.1103/PhysRevLett.123.112002

[P324-2019] "Galaxies in X-ray selected clusters and groups in Dark Energy Survey data - II. Hierarchical Bayesian modelling of the red-sequence galaxy luminosity function"

Zhang, Y.; Miller, C. J.; Rooney, P.; **Sobreira, F.***; et. al.; DES Collaboration

Using similar to 100 X-ray selected clusters in the Dark Energy Survey Science Verification data, we constrain the luminosity function (LF) of cluster red-sequence galaxies as a function of redshift. This is the first homogeneous optical/X-ray sample large enough to constrain the evolution of the LF simultaneously in redshift (0.1 < z < 1.05) and cluster mass (13.5 <= log(10) (M-200crit) similar to< 15.0). We pay particular attention to completeness issues and the detection limit of the galaxy sample. We then apply a hierarchical Bayesian model to fit the cluster galaxy LFs via a Schechter function, including its characteristic break (m*) to a faint end power-law slope (alpha).

Our method enables us to avoid known issues in similar analyses based on stacking or binning the clusters. We find weak and statistically insignificant (similar to 1.9 sigma) evolution in the faint end slope alpha versus redshift. We also find no dependence in alpha or m* with the X-ray inferred cluster masses. However, the amplitude of the LF as a function of cluster mass is constrained to similar to 20 per cent precision. As a by-product of our algorithm, we utilize the correlation between the LF and cluster mass to provide an improved estimate of the individual cluster masses as well as the scatter in true mass given the X-ray inferred masses. This technique can be applied to a larger sample of X-ray or optically selected clusters from the Dark Energy Survey, significantly improving the sensitivity of the analysis.

MONTHLY NOTICES OF THE ROYAL ASTRONOMICAL SOCIETY 488[1], 1-17, 2019. DOI: 10.1093/mnras/stz1612

[P325-2019] "Gold Nanoparticles for X-ray Microtomography of Neurons"

Depannemaecker, D.; Santos, L. E. C.; de Almeida, A. C, G.; **Ferreira, G. B. S.*; Barald, G. L.***; Miqueles, E. X.; de Carvalho, M.; Costa, G. S. R.; Marques, M. J. G.; Scorza, C. A.; **Rinkel, J.***

Commonly used methods to visualize the biological structure of brain tissues at subcellular resolution are confocal microscopy and two-photon microscopy. Both require slicing the sample into sections of a few tens of micrometers. The recent developments in X-ray microtomography enable three-dimensional imaging at sub-micrometer and isotropic resolution with larger biological samples. In this work, we developed and compared original microtomography methods and staining protocols to improve the contrast for in vitro mouse neuron imaging. Using Golgi's method to stain neurons randomly, we imaged the whole set of mouse brain structures. For specific and nonrandom neuron labeling, we conjugated 20 nm gold nanoparticles to antibodies used in the immunohistochemistry (IHC) method, using anti-NeuN to label specifically neuronal nuclei. We applied an original subtraction dual-energy method for microtomography in the vicinity of the Au L-III absorption edge and compared image reconstructions to confocal microscopy images acquired on the same samples. The results show the possibility to characterize the 3D entire brain structure of mice. They demonstrated a high contrast and neuron detection improvement by applying the dual-energy method coupled to IHC staining.

ACS CHEMICAL NEUROSCIENCE 10[8], 3404-3408, 2019. DOI: 10.1021/acschemneuro.9b00290

[P326-2019] "Influence of silver electrochemically deposited onto zinc oxide seed nanoparticles on the photoelectrochemical performance of zinc oxide nanorod films"

Aranda, A.; **Landers, R.***; Carnelli, P.; Candal, R.; Alarcon, H.; Rodriguez, J.

The present article examines the synthesis and characterization of zinc oxide nanorods grown on zinc oxide and silver nanoparticle seeds. Zinc oxide seeds were electrodeposited on a support of fluorine-doped tin oxide glass and heat-treated at 380 degrees C. Silver nanoparticles were then deposited on this substrate, which was heat-treated at 160 degrees C. Their presence was confirmed using ultraviolet-visible spectroscopy, by observing an absorption peak around 400 nm, corresponding to surface plasmon resonance. Growth of zinc oxide nanorods was achieved in a chemical bath at 90 degrees C. The obtained films were analyzed by cyclic voltammetry, X-ray diffraction, and scanning electron microscopy. They consisted of zinc oxide with a Wurtzite-type crystal structure, arranged as nanorods of 50 nm. X-ray photoelectron spectroscopy exhibits peaks attributed to silver (0) and to the formation of silver oxide on the silver nanoparticle surface. In addition, two types of oxygen (O 1 s) were observed: oxygen from the crystalline network (O-2) and chemisorbed oxygen (-OH), for the seed and the nanorod films, respectively. The nanorods grown on zinc oxide seeds with silver deposits had a round shape and greater photoactivity than those grown without silver. This difference is attributed to the additional reflection that silver provides to the light reaching the film, thereby increasing the photogeneration from the charge carriers.

NANOMATERIALS AND NANOTECHNOLOGY 9, 1847980419844363, 2019. DOI: 10.1177/1847980419844363

[P327-2019] "Island growth mode in pulsed laser deposited ferroelectric BaTiO3 thin films: The role of oxygen pressure during deposition"

Estrada, F. R.; de Moraes, L. G. M.; **Vital, F. L. A.*; Neme, M. D.***; Schio, P.; Mori, T. J. A.; Cezar, J. C.

Pulsed laser deposition is widely used to grow BaTiO3 thin films. We investigated the influence of oxygen pressure during growth on the topography, microstructure, and roughness of ferroelectric epitaxial BaTiO3 thin films. It also presented an analysis of the epitaxial growth mode and defects throughout the film thickness using aberration-corrected transmission electron microscopy. Although ferroelastic (twin boundary) domain walls are absent, several misfit dislocations were observed and might be the primary cause of the observed island growth mode.

FERROELECTRICS 545[1](SI), 39-44, 2019. DOI: 10.1080/00150193.2019.1621709

[P328-2019] "Large magnetocaloric effect in ErCoSn driven by metamagnetic phase transition and short-range ferromagnetic correlations"

Souza, R. L.; **Monteiro, J. C. B.***; dos Santos, A. O.; **Cardoso, L. P.***; da Silva, L. M.

Here, we report the results of structural, magnetic, thermal and magnetocaloric properties of ErCoSn compound. The compound undergoes an antiferromagnetic (AFM) ordering around T-N = 4.6 K and magnetic correlation is observed above T-N, up to T = 11 K. Below T-N, a spin-glass state was observed for ErCoSn due to an apparent coexistence of ferromagnetic (FM) interaction with long-range AFM order. External applied magnetic field induces a first-order-like metamagnetic phase transition from AFM to FM state that is responsible for the large values of the maximum isothermal entropy change (-Delta(max)(M) = 16.5 J/kgK@50kOe) and adiabatic temperature change (Delta T-ad = 8.2 K). Furthermore, short--range ferromagnetic correlation above T-N contributes to the widening of -Delta S-M and Delta T-ad peaks as well as the increase of the ErCoSn compound refrigerant capacity. The results indicate attractive properties of this compound for magnetic refrigeration at cryogenic temperatures.

JOURNAL OF MAGNETISM AND MAGNETIC MATERIALS 492, UNSP 165653, 2019. DOI: 10.1016/j.jmmm.2019.165653

[P329-2019] "Low temperature sulfonation of acai stone biomass derived carbons as acid catalysts for esterification reactions"

Araujo, R. O.; Chaar, J. da S.; Queiroz, L. S.; da Rocha Filho, G. N.; da Costa, C. E. F.; da Silva, G. C. T.; **Landers, R.***; Costa, M. J. F.; Goncalves, A. A. S.; de Souza, L. K. C.

Heterogeneous acid catalysts derived from acai stone (Euterpe oleracea Mart), a large-scale residue biomass, were synthesized by partial carbonization followed by sulfonation within a short preparation time under controllable conditions. Their catalytic activity was tested in the esterification reaction of oleic acid with alcohols, with varying chain-lengths, and with a modified edible oil with high fatty acid content. The sulfonated carbon materials were characterized by X-ray diffraction (XRD), scanning electron microscopy coupled with an EDS system for elemental mapping (SEM-EDS), thermogravimetry (TG), infrared spectroscopy (FT-IR), low-temperature N-2 sorption, and X-ray photoelectron spectroscopy (XPS). The reaction conditions and catalyst preparation were systematically investigated with respect to carbonization and sulfonation temperatures, reaction temperature and time, reactants' molar ratio, catalyst loading, alcohol type, and recyclability. A low carbonization temperature created carbon materials with surface features that favored the anchoring of sulfonic groups, in turn providing desirable sulfonation under mild temperatures. After optimization of the reaction conditions, a yield of 93% was obtained when 5% catalyst loading was used to convert a 1:12 oleic acid to methanol molar ratio at 100 degrees C for 1 h. Comparatively, the uncatalyzed reaction yielded only 11% conversion. The sulfonated carbon catalyst was tested in the esterification of soybean oil that was modified with 20% oleic acid to reduce the quality of feedstock and simulate harsh conditions; the catalyzed reaction showed yields up to 80%. Moreover, the synthesized catalyst was stable for up to three reaction cycles, displaying a decrease in efficiency of only 8%. This study shows promising results for obtaining sulfonated carbon catalysts from acai stone biomass, thereby potentially solving one of the major environmental problems in the Amazon region and providing a sustainable alternative for fuel production.

ENERGY CONVERSION AND MANAGEMENT 196, 821-830, 2019. DOI: 10.1016/j.enconman.2019.06.059

[P330-2019] "Magnetocaloric properties of (Gd1-xErx)(3)Ru alloys and their composites"

Monteiro, J. C. B.*; Gandra, F. G.*

We present magnetization, specific heat and magnetocaloric effect results for the compounds (Gd1-xErx)(3)Ru, with x = 0.05, 0.1, 0.2 and 1. As Er concentration increases we observe a significant reduction of the transition temperature from 52 K to 8.1 K and a change from first order ferromagnetic to second order antiferromagnetic behavior. Despite the magnetic arrangement changes, the magnetocaloric potential remains high and a composite formed with these compounds is proposed to achieve temperatures of 20 K starting from nitrogen boiling point. The magnetic entropy variation and adiabatic temperature change of the composite were directly measured presenting a plateau between 20 K and 77 K with values higher than 6 J/kg.K and 3 K respectively for a magnetic field variation of 5 T.

JOURNAL OF ALLOYS AND COMPOUNDS 803, 1178-1183, 2019. DOI: 10.1016/j.jallcom.2019.06.265

[P331-2019] "Measurement of associated production of a W boson and a charm quark in proton-proton collisions at root s=13 Tev"

Sirunyan, A. M.; Tumasyan, A.; Adam, W.; **Chinellato, J. A.*; Tonelli Manganote, E. J.***; et. al.; CMS Collaboration

Measurements are presented of associated production of a W boson and a charm quark (W + c) in proton-proton collisions at a center-of-mass energy of 13 TeV. The data correspond to an integrated luminosity of 35.7 fb(-1) collected by the CMS experiment at the CERN LHC. The W bosons are identified by their decay into a muon and a neutrino. The charm quarks are tagged via the full reconstruction of D* (2010)(+/-) mesons that decay via D*(2010)(+/-) D-0 + pi(+/-) -> K--/+ + pi(+/-) + pi(+/-). A cross section is measured in the fiducial region defined by the muon transverse momentum p(T)(mu) > 26 GeV, muon pseudorapidity vertical bar eta(mu)vertical bar < 2.4, and charm quark transverse momentum p(T)(c) > 5 GeV. The inclusive cross section for this kinematic range is sigma(W + c) = 1026 +/- 31(stat)(-72)(+76) pb. The cross section is also measured differentially as a function of the pseudorapidity of the muon from the W boson decay. These measurements are compared with theoretical predictions and are used to probe the strange quark content of the proton.

EUROPEAN PHYSICAL JOURNAL C 79[3], 269, 2019. DOI: 10.1140/epjc/s10052-019-6752-1

[P332-2019] "Measurement of B-s(0) meson production in pp and PbPb collisions at root S-NN=5.02 TeV"

Sirunyan, A. M.; Tumasyan, A.; Adam, W.; **Chinellato, J. A.,*; Tonelli Manganote, E. J.***; et. al.; CMS Collaboration

The production cross sections of B-s(0) mesons and charge conjugates are measured in proton-proton (pp) and PbPb collisions via the exclusive decay channel B-s(0)-> J/ psi phi ->mu(+) mu(-) K+K- at a center-of-mass energy of 5.02 TeV per nucleon pair and within the rapidity range vertical bar y vertical bar < 2.4 using the CMS detector at the LHC. The pp measurement is performed as a function of transverse momentum (P-T) of the B-s(0), mesons in the range of 7 to 50 GeV/c and is compared to the predictions of perturbative QCD calculations. The B s production yield in PbPb collisions is measured in two F t intervals, 7 to 15 and 15 to 50 GeV/c, and compared to the yield in pp collisions in the same kinematic region. The nuclear modification factor (R-AA) is found to be 1.5 +/- 0.6(stat) +/- 0.5(syst) for 7-15 GeV/c, and 0.87 +/- 0.30(stat) +/- 0.1 7(syst) for 15-50 GeV/c, respectively. Within current uncertainties, the B-s(0) results are consistent with models of strangeness enhancement, and suppression by parton energy loss, as observed for the B+ mesons.

PHYSICS LETTERS B 796, 168-190, 2019. DOI: 10.1016/j.physletb.2019.07.014

[P333-2019] "Measurement of electroweak WZ boson production and search for new physics in WZ plus two jets events in pp collisions at root s=13 TeV"

Sirunyan, A. M.; Tumasyan, A.; Adam, W.; **Chinellato, J. A.*; Tonelli Manganote, E. J.***; et. al.; CMS Collaboration

A measurement of WZ electroweak (EW) vector boson scattering is presented. The measurement is performed in the leptonic decay modes WZ -> l nu l'l', where l, l' = e, mu. The analysis is based on a data sample of proton-proton collisions at root s = 13 TeV at the LHC collected with the CMS detector and corresponding to an integrated luminosity of 35.9 fb(-1) . The WZ plus two jet production cross section is measured in fiducial regions with enhanced contributions from EW production and found to be consistent with standard model predictions. The EW WZ production in association with two jets is measured with an observed (expected) significance of 2.2 (2.5) standard deviations. Constraints on charged Higgs boson production and on anomalous quartic gauge couplings in terms of dimension--eight effective field theory operators are also presented.

PHYSICS LETTERS B 795, 281-307, 2019. DOI: 10.1016/j.physletb.2019.05.042

[P334-2019] "Measurement of electroweak WZ boson production and search for new physics in WZ plus two jets events in pp collisions at root s=13 TeV"

Sirunyan, A. M.; Tumasyan, A.; Adam, W.; **Chinellato, J. A.*; Tonelli Manganote, E. J.***; et. al.; CMS Collaboration

A measurement of WZ electroweak (EW) vector boson scattering is presented. The measurement is performed in the leptonic decay modes WZ -> l nu l'l', where l, l' = e, mu. The analysis is based on a data sample of proton-proton collisions at root s = 13 TeV at the LHC collected with the CMS detector and corresponding to an integrated luminosity of 35.9 fb(-1) . The WZ plus two jet production cross section is measured in fiducial regions with enhanced contributions from EW production and found to be consistent with standard model predictions. The EW WZ production in association with two jets is measured with an observed (expected) significance of 2.2 (2.5) standard deviations. Constraints on charged Higgs boson production and on anomalous quartic gauge couplings in terms of dimension--eight effective field theory operators are also presented.

PHYSICS LETTERS B 795, 281-307, 2019. DOI: 10.1016/j.physletb.2019.05.042

[P335-2019] "Measurement of jet radial profiles in Pb-Pb collisions at root s(NN)=2.76 TeV"

Acharya, S.; Adamova, D.; Adhya, S. P.; **Albuquerque, D. S. D.*; Chinellato, D. D.*; De Souza, R. D.*; Takahashi, J.***; et. al.; ALICE Collaboration

The jet radial structure and particle transverse momentum (p(T)) composition within jets are presented in centrality-selected Pb-Pb collisions at root s(NN) = 2.76 TeV. Track-based jets, which are also called charged jets, were reconstructed with a resolution parameter of R = 0.3 at midrapidity vertical bar eta(chjet)vertical bar < 0.6 for transverse momenta P-T,P-(ch jet) = 30-120 GeV/c. Jet-hadron correlations in relative azimuth and pseudorapidity space (Delta phi/Delta eta) are measured to study the distribution of the associated particles around the jet axis for different p(T, assoc)-ranges between 1 and 20 GeV/c. The data in Pb-Pb collisions are compared to reference distributions for pp collisions, obtained using embedded PYTHIA simulations. The number of high-p(T) associate particles (4 < p(T,assoc) < 20 GeV/c) in Pb-Pb collisions is found to be suppressed compared to the reference by 30 to 10%, depending on centrality. The radial particle distribution relative to the jet axis shows a moderate modification in Pb-Pb collisions with respect to PYTHIA. High-p(T) associate particles are slightly more collimated in Pb-Pb collisions compared to the reference, while low-p(T) associate particles tend to be broadened. The results, which are presented for the first time down to p(T, chjet) = 30 GeV/c in Pb-Pb collisions, are compatible with both previous jet-hadron-related measurements from the CMS Collaboration and jet shape measurements from the ALICE Collaboration at higher p(T), and add further support for the established picture of in-medium parton energy loss.

PHYSICS LETTERS B 796, 204-219, 2019. DOI: 10.1016/j.physletb.2019.07.020

[P336-2019] "Measurement of the branching ratio of pi(0) Dalitz decay using K-L -> pi(0)pi(0)pi(0) decays"

Abouzaid, E.; Arenton, M.; Barker, A. R.; **Escobar, C. O.*; Gomes, R. A.***; et. al.

We present a measurement of B(pi(0) -> e(+)e(-)gamma)/B(pi(0) -> gamma gamma), the Dalitz branching ratio, using data taken in 1999 by the E832 KTeV experiment at Fermi National Accelerator Laboratory. We use neutral pions from fully reconstructed K-L decays in flight; the measurement is based on similar to 60 thousand K-L -> pi(0)pi(0)pi(0) -> gamma gamma gamma gamma e(+) e(-)gamma decays. We normalize to K-L -> pi(0)pi(0)pi(0) -> 6 gamma decays. We find B(pi(0) -> e(+)e(-)gamma)/B(pi(0) -> gamma gamma) (m(e+e-) > 15 MeV/c(2)) = [3.920 +/- 0.016(stat) +/- 0.036(syst)] x 10(-3). Using the Mikaelian and Smith prediction for the e(+)e(-) mass spectrum, we correct the result to the full e(+)e(-) mass range. The corrected result is B(pi(0) -> e(+)e(-)gamma)/B(pi(0) -> gamma gamma) = [1.1559 +/- 0.0047(stat) +/- 0.0106(syst)]%. This result is consistent with previous measurements, and the uncertainty is a factor of 3 smaller than any previous measurement.

PHYSICAL REVIEW D 100[3], 032003, 2019. DOI: 10.1103/PhysRevD.100.032003

[P337-2019] "Measurement of the production of charm jets tagged with D-0 mesons in pp collisions at root s=7 TeV"

Acharya, S.; Acosta, F. T.; Adam, J.; **Albuquerque, D. S. D.*; Chinellato, D. D.*; De Souza, R. D.*; Takahashi, J.***; et.al.; ALICE Collaboration

The production of charm jets in proton-proton collisions at a center-of-mass energy of p s = 7TeV was measured with the ALICE detector at the CERN Large Hadron Collider. The measurement is based on a data sample corresponding to a total integrated luminosity of 6: 23 nb, collected using a minimum--bias trigger. Charm jets are identi fi ed by the presence of a D 0 meson among their constituents. The D 0 mesons are reconstructed from their hadronic decay D 0 ! K. The D 0 -meson tagged jets are reconstructed using tracks of charged particles (track-based jets) with the anti-k T algorithm in the jet transverse momentum range 5 < p ch T;jet < 30 GeV= c and pseudorapidity jjetj < 0: 5. The fraction of charged jets containing a D 0 -meson increases with p ch T;jet from 0: 042 0: 004 (stat) 0: 006 (syst) to 0: 080 0: 009 (stat) 0: 008 (syst). The distribution of D 0 -meson tagged jets as a function of the jet momentum fraction carried by the D 0 meson in the direction of the jet axis (z ch jj) is reported for two ranges of jet transverse momenta, 5 < p ch T;jet < 15 GeV= c and 15 < p ch T;jet < 30 GeV= c in the intervals 0: 2 < z ch jj < 1: 0 and 0: 4 < z ch jj < 1: 0, respectively. The data are compared with results from Monte Carlo event generators (PYTHIA 6, PYTHIA 8 and Herwig 7) and with a Next-to-Leading-Order perturbative Quantum Chromodynamics calculation, obtained with the POWHEG method and interfaced with PYTHIA 6 for the generation of the parton shower, fragmentation, hadronisation and underlying event.

JOURNAL OF HIGH ENERGY PHYSICS 8, 133, 2019. DOI: 10.1007/JHEP08(2019)133

[P338-2019] "Methods for cluster cosmology and application to the SDSS in preparation for DES Year 1 release"

Costanzi, M.; Rozo, E.; Simet, M.; **Sobreira, F.***; et. al.; DES Collaboration

We implement the first blind analysis of cluster abundance data to derive cosmological constraints from the abundance and weak lensing signal of redMaPPer clusters in the Sloan Digital Sky Survey (SDSS). We simultaneously fit for cosmological parameters and the richness-mass relation of the clusters. For a flat Lambda cold dark matter cosmological model with massive neutrinos, we find . This value is both consistent and competitive with that derived from cluster catalogues selected in different wavelengths. Our result is also consistent with the combined probes analyses by the Dark Energy Survey (DES), the Kilo-Degree Survey (KiDS), and with the cosmic microwave background (CMB) anisotropies as measured by Planck.

We demonstrate that the cosmological posteriors are robust against variation of the richness-mass relation model and to systematics associated with the calibration of the selection function. In combination with baryon acoustic oscillation data and big bang nucleosynthesis data (Cooke etal.), we constrain the Hubble rate to be h= 0.66 +/- 0.02, independent of the CMB. Future work aimed at improving our understanding of the scatter of the richness-mass relation has the potential to significantly improve the precision of our cosmological posteriors. The methods described in this work were developed for use in the forthcoming analysis of cluster abundances in the DES. Our SDSS analysis constitutes the first part of a staged-unblinding analysis of the full DES data set.

MONTHLY NOTICES OF THE ROYAL ASTRONOMICAL SOCIETY 488[4], 4779-4800, 2019. DOI: 10.1093/mnras/stz1949

[P339-2019] "Mixing the immiscible through high-velocity mechanical impacts: an experimental and theoretical study"

Malviya, K. D.; **Oliveira, E. F.*; Autreto, P. A. S.***; Ajayan, P. M.; **Galvao, D. S.***; Tiwary, C. S.; Chattopadhyay, K.

In two-component metallic systems, thermodynamic immiscibility leads to phase separation such as in two-phase eutectic compositional alloys. The limit of the immiscibility of component elements under non-equilibrium conditions have been explored, but achieving complete miscibility and formation of single phase microstructures in eutectic alloys would be unprecedented. Here, we report that during the low-temperature ball milling that provides high energy impact, complete mixing of phases can occur in immiscible Ag-Cu eutectic alloys. From combined theoretical and experimental studies, we show that impact can produce solid solutions of Ag-Cu nanoparticles of eutectic composition. Our results show that phase diagrams of low dimensional materials under non-equilibrium conditions remain unexplored and could lead to new alloy microstructures drastically different from their bulk counterparts.

JOURNAL OF PHYSICS D-APPLIED PHYSICS 52[44], 445304, 2019. DOI: 10.1088/1361-6463/ab36d1

[P340-2019] "Modular structure in C. elegans neural network and its response to external localized stimuli"

Moreira, C. A.*; de Aguiar, M. A. M.*

Synchronization plays a key role in information processing in neuronal networks. Response of specific groups of neurons are triggered by external stimuli, such as visual, tactile or olfactory inputs. Neurons, however, can be divided into several categories, such as by physical location, functional role or topological clustering properties. Here we study the response of the electric junction C. elegans network to external stimuli using the partially forced Kuramoto model and applying the force to specific groups of neurons. Stimuli were applied to three topological modules, two ganglia, specified by their anatomical localization, and to the functional groups composed of all sensory and motoneurons. We found that topological modules do not contain purely anatomical groups or functional classes, corroborating previous results, and that stimulating different classes of neurons lead to very different responses, measured in terms of synchronization and phase velocity correlations. In all cases the modular structure hindered full synchronization, protecting the system from seizures. The responses to stimuli applied to topological and functional modules showed pronounced patterns of correlation or anti-correlation with other modules that were not observed when the stimulus was applied to a ganglion with mixed functional neurons.

PHYSICA A-STATISTICAL MECHANICS AND ITS APPLICATIONS 533, UNSP 122051, 2019. DOI: 10.1016/j.physa.2019.122051

[P341-2019] "Nanostructured lipid carriers loaded with free phytosterols for food applications"

Santos, V. da S.; Braz, B. B.; Silva, A. A.; **Cardoso, L. P.***; Ribeiro, A. P. B.; Santana, M. H. A.

The objective of this study was to develop nanostructured lipid carriers (NLCs) with free phytosterols (FP) using conventional fats and oils. Lipid matrices (LMs) and NLCs were produced with high oleic sunflower oil, fully hydrogenated canola (CA) and crambe (CR) oils by high-pressure homogenization (HPH). The NLCs were evaluated for hydrodynamic diameter (Z-ave), polydispersity index (PDI), and zeta potential (ZP). The melting behavior and polymorphism were investigated for both, the LMs and NLCs. The NLCs presented particle sizes ranging from 148.23 to 342.10 nm, PDI from 0.275 to 0.481, and ZP between -22.27 and -29.70 mV. The NLCs presented higher thermal resistance than that of the LMs. The use of CA and CR separately in the NLC formulations favored the incorporation of FP. The LMs and NLCs presented crystals in beta-form and in mixtures of beta' and beta forms. The developed NLCs can be used for food enrichment, such as spreads, margarine, and beverages.

FOOD CHEMISTRY 298, UNSP 125053, 2019. DOI: 10.1016/j.foodchem.2019.125053

[P342-2019] "Non-Markovian Exciton-Phonon Interactions in Core-Shell Colloidal Quantum Dots at Femtosecond Timescales"

Liu, A.; Almeida, D. B.; Bae, W. K.; **Padilha, L. A.***; Cundiff, S. T.

We perform two-dimensional coherent spectroscopy on CdSe/CdZnS core-shell colloidal quantum dots at cryogenic temperatures. In the two-dimensional spectra, sidebands due to electronic coupling with CdSe lattice LO-phonon modes are observed to have evolutions deviating from the exponential dephasing expected from Markovian spectral diffusion, which is instantaneous and memoryless. Comparison to simulations provides evidence that LO-phonon coupling induces energy-gap fluctuations on the finite timescales of nuclear motion. The femtosecond resolution of our technique probes exciton dynamics directly on the timescales of phonon coupling in nanocrystals.

PHYSICAL REVIEW LETTERS 123[5], 057403, 2019. DOI: 10.1103/PhysRevLett.123.057403

[P343-2019] "One-dimensional charged kaon femtoscopy in p-Pb collisions at root s(NN)=5.02 TeV"

Acharya, S.; Adamova, D.; Adhya, S. P.; A**lbuquerque, D. S. D.*; Chinellato, D. D.*; De Souza, R. D.*; Takahashi, J.*;** et. al.; ALICE Collaboration

The correlations of identical charged kaons were measured in p-Pb collisions at root s(NN) = 5.02 TeV by the ALICE experiment at the LHC. The femtoscopic invariant radii and correlation strengths were extracted from one-dimensional kaon correlation functions and were compared with those obtained in pp and Pb-Pb collisions at root s = 7 TeV and root s(NN) = 2.76 TeV, respectively. The presented results also complement the identical-pion femtoscopic data published by the ALICE collaboration. The extracted radii increase with increasing charged-particle multiplicity and decrease with increasing pair transverse momentum. At comparable multiplicities, the radii measured in p-Pb collisions are found to be close to those observed in pp collisions. The obtained femtoscopic parameters are reproduced by the EPOS 3 hadronic interaction model and disfavor models with large initial size or strong collective expansion at low multiplicities.

PHYSICAL REVIEW C 100[2], 024002, 2019. DOI: 10.1103/PhysRevC.100.024002

[P344-2019] "Optical-force laws for guided light in linear media"

Fernandes, T. F. D.; **de Assis, P. L.***

The mechanical response of transparent materials to optical forces is a topic that concerns a wide range of fields, from the manipulation of biological material by optical tweezers to the design of nano-optomechanical systems. However, the fundamental aspects of such forces have always been surrounded by controversies, and several different formulations have been proposed. In this paper, we propose a general stress tensor formalism to put all optical forces in a consistent presentation that allows us to study how different predictions emerge, and use the specific case of light propagating as a superposition of guided modes in lossless dielectric waveguides as a physical example. We use this formalism to calculate optical forces for straight and curved waveguide sections and all possible excitation configurations for a given set of coupled eigenmodes, and then compare the results for each of the known proposed optical-force laws in a framework that permits distinguishing where there will be differences between the force laws proposed. The general formalism also allows us to show that proper use of the divergence theorem is crucial to account for all force terms, many of which vanish if the procedure most commonly used is applied for situations other than eigenmodes in straight waveguides in vacuum. Finally, it is known that discrepancies in the predicted forces arise from the incompleteness of each stress tensor with respect to the total-energy-momentum tensor of the system. A better understanding of how different stress tensors predict very different forces for certain waveguide geometries should open a pathway to identifying how to properly assemble the full tensor, as well as for experimental tests to confirm the predictions.

PHYSICAL REVIEW A 100[1], 013835, 2019. DOI: 10.1103/PhysRevA.100.013835

[P345-2019] "Oxygen Reduction on Methanol-Tolerant Carbon-Supported PtxSy Nanoparticles Prepared by a Single--Step Low-Temperature Method"

Carbonio, E. A.; Rodrigues Filho, U. P.; Mesquita, A.; **Landers, R.***; Gonzalez, E. R.

In direct methanol fuel cells (DMFCs), the methanol crossover from the anode to the cathode is a major cause of power density loss because of the overpotential arising due to the parasitic reaction of methanol oxidation at the cathode. Catalysts modified with S have shown better methanol tolerance; however, the preparation routes often require high temperatures or pressures and very long times, making these expensive and unlikely to be used in large scale. Here, we report on a single-step low-temperature method used to prepare a carbon-supported PtxSy catalyst. Moreover, we show that the catalyst shows lower depolarization in the presence of methanol and study the effect of reductive thermal treatment and electrochemical potential cycling.

ELECTROCATALYSIS 10[5], 516-523, 2019. DOI: 10.1007/s12678-019-00522-9

[P346-2019] "Physical approach for a quantitative analysis of the phytosterols in free phytosterol-oil blends by X-ray Rietveld method"

Gomes Silva, M.; Santos, V. S.; Fernandes, G. D.; **Calligaris, G. A.***; Santana, M. H. A.; **Cardoso, L. P.***; Ribeiro, A. P. B.

This study investigates and compares the thermal phase transition and crystallization characteristics of a commercial food grade free phytosterol blend (FP) with a stigmasterol analytical standard (SS), the FP behavior in a food model system after its addition to high oleic sunflower oil (HOSO). The properties of the FP:HOSO blends were studied by differential scanning calorimetry, solid content, crystal morphology, and X-ray diffraction (XRD) measurements. The Rietveld method (RM) was applied associated with the XRD measurements to support phase analysis and the study of crystallinity degree. The materials were also characterized by means of chemical composition, such as fatty acids and triacylglycerol profiles, for HOSO, and phytosterol profile, for FP. Regarding phase behavior and crystallinity properties, FP has very similar characteristics to SS. The thermal behavior of FP:HOSO blends has two characteristic peaks, one from FP and the other from HOSO. The similarity reported in the literature between the diffraction pattern of FP and pure phytosterols is a positive characteristic for FP. A high FP concentration resulted in high supersaturation and thus the formation of small crystals. The incorporation of HOSO reduced of the large agglomeration of FP crystals and the dispersion crystalline aggregates (spherulites) of FP crystals. The application of RM in FP:HOSO blends to quantify the crystalline and amorphous phases was successfully used. The application has provided the expected value for these phases, according to the same experimental mass ratio of the blends, thereby validating the applicability of this approach in this type of material.

FOOD RESEARCH INTERNATIONAL 124[SI], 2-15, 2019. DOI: 10.1016/j.foodres.2019.04.006

[P347-2019] "Production of muons from heavy-flavour hadron decays in pp collisions at root s=5.02 TeV"

Acharya, S.; Adamova, D.; Adhya, S. P.; **Albuquerque, D. S. D.*; Chinellato, D. D.*; De Souza, R. D.*; Takahashi, J.***; et. al.; Al Alikhanyan Natl Sci Lab

Production cross sections of muons from semi-leptonic decays of charm and beauty hadrons were measured at forward rapidity ($2.5 < y < 4$) in proton-proton (pp) collisions at a centre-of--mass energy root s = 5.02 TeV with the ALICE detector at the CERN LHC. The results were obtained in an extended transverse momentum interval, $2 < p(T) < 20$ GeV/c, and with an improved precision compared to previous measurements performed in the same rapidity interval at centre-of-mass energies root s = 2.76 and 7 TeV. The p(T)- and y-differential production cross sections as well as the p(T)-differential production cross section ratios between different centre-of-mass energies and different rapidity intervals are described, within experimental and theoretical uncertainties, by predictions based on perturbative QCD.

JOURNAL OF HIGH ENERGY PHYSICS 9, 008, 2019. DOI: 10.1007/JHEP09(2019)008

[P348-2019] "Quantum decoherence effects in neutrino oscillations at DUNE"

Gomes, G. B.*; Forero, D. V.*; Guzzo, M. M.*; de Holanda, P. C.*; Oliveira, R. L. N.*

In this work, we analyze quantum decoherence in neutrino oscillations considering the open quantum system framework and oscillations through matter for three-neutrino families. Taking the Deep Under-ground Neutrino Experiment as a case study, we performed sensitivity analyses for two neutrino flux configurations, finding sensitivity limits for the decoherence parameters. We also offer a physical interpretation for a new peak which arises at the nu(e) appearance probability with decoherence. The sensitivity limits found for the decoherence parameters are Gamma(21) <= 1.2 x 10(-23) GeV and Gamma(32) <= 7.7 x 10(-15) GeV at 90% C.L.

PHYSICAL REVIEW D 100[5], 055023, 2019. DOI: 10.1103/PhysRevD.100.055023

[P349-2019] "Raman spectroscopy of dorsal root ganglia from streptozotocin-induced diabetic neuropathic rats submitted to photobiomodulation therapy"

Vieira, W. F.; de Magalhaes, S. F.; Farias, F. H.; **de Thomaz, A. A.***; Parada, C. A.

In this study, we used Raman spectroscopy as a new tool to investigate pathological conditions at the level of chemical bond alterations in biological tissues. Currently, there have been no reports on the spectroscopic alterations caused by diabetic neuropathy in the dorsal root ganglia (DRG). DRG are a target for the treatment of neuropathic pain, and the need for more effective therapies is increasing. Photobiomodulation therapy (PBMT) through infrared low-level laser irradiation (904 nm) has shown analgesic effects on the treatment of neuropathy. Thus, the aim of this study was to use Raman spectroscopy to characterize the spectral DRG identities of streptozotocin (STZ)-induced diabetic neuropathic (hyperalgesic) rats and to study the influence of PBMT over such spectra. Characteristic DRG peaks were identified at 2704, 2850, 2885, 2940, 3061 and 3160 cm(-1), whose assignments are CH2/CH3 symmetric/asymmetric stretches, and CH vibrations of lipids and proteins. DRG from hyperalgesic rats showed an increased normalized intensity of 2704, 2850, 2885 and 3160 cm(-1). These same peaks had their normalized intensity reduced after PBMT treatment, accompanied by an anti-hyperalgesic effect. Raman spectroscopy was able to diagnose spectral alterations in DRG of hyperalgesic rats and the PBMT reduced the intensity of hyperalgesia and the altered Raman spectra.

JOURNAL OF BIOPHOTONICS UNSP e201900135, 2019. DOI: 10.1002/jbio.201900135

[P350-2019] "Resistivity near a nematic quantum critical point: Impact of acoustic phonons"

de Carvalho, V. S.*; Fernandes, R. M.

We revisit the issue of the resistivity of a two-dimensional electronic system tuned to a nematic quantum critical point (QCP), focusing on the nontrivial impact of the coupling to the acoustic phonons. Due to the unavoidable linear coupling between the electronic nematic order parameter and the lattice strain fields, long-range nematic interactions mediated by the phonons emerge in the problem. By solving the semiclassical Boltzmann equation in the presence of scattering by impurities and nematic fluctuations, we determine the temperature dependence of the resistivity as the nematic QCP is approached. One of the main effects of the nematoelastic coupling is to smooth the electronic nonequilibrium distribution function, making it approach the simple cosine angular dependence even when the impurity scattering is not too strong. We find that at temperatures lower than a temperature scale set by the nematoelastic coupling, the resistivity shows the T-2 behavior characteristic of a Fermi liquid. This is in contrast to the T-4/3 low-temperature behavior expected for a lattice-free nematic quantum critical point. More importantly, we show that the effective resistivity exponent alpha(eff)(T) in rho(T) - rho(0) similar to T-alpha eff(T) displays a pronounced temperature dependence, implying that a nematic QCP cannot generally be characterized by a simple resistivity exponent. We discuss the implications of our results to the interpretation of experimental data, particularly in the nematic superconductor FeSe1-xSx.

PHYSICAL REVIEW B 100[11], 115103, 2019. DOI: 10.1103/PhysRevB.100.115103

[P351-2019] "Revealing biases in the sampling of ecological interaction networks"

Aguiar, M. A. M.*; Newman, E. A.; Pires, M. M.; Yeake, J. D.; Boettiger, C.; Burkle, L. A.; Gravel, D.; Guimaraes, P. R.; O'Donnell, J. L.; Poisot, T.; Fortin, M. J.; Hembry, D. H.

The structure of ecological interactions is commonly understood through analyses of interaction networks. However, these analyses may be sensitive to sampling biases with respect to both the interactors (the nodes of the network) and interactions (the links between nodes), because the detectability of species and their interactions is highly heterogeneous. These ecological and statistical issues directly affect ecologists' abilities to accurately construct ecological networks. However, statistical biases introduced by sampling are difficult to quantify in the absence of full knowledge of the underlying ecological network's structure. To explore properties of large-scale ecological networks, we developed the software EcoNetGen, which constructs and samples networks with predetermined topologies. These networks may represent a wide variety of communities that vary in size and types of ecological interactions. We sampled these networks with different mathematical sampling designs that correspond to methods used in field observations. The observed networks generated by each sampling process were then analyzed with respect to the number of components, size of components and other network metrics. We show that the sampling effort needed to estimate underlying network properties depends strongly both on the sampling design and on the underlying network topology. In particular, networks with random or scale-free modules require more complete sampling to reveal their structure, compared to networks whose modules are nested or bipartite. Overall, modules with nested structure were the easiest to detect, regardless of the sampling design used. Sampling a network starting with any species that had a high degree (e.g., abundant generalist species) was consistently found to be the most accurate strategy to estimate network structure. Because high-degree species tend to be generalists, abundant in natural communities relative to specialists, and connected to each other, sampling by degree may therefore be common but unintentional in empirical sampling of networks. Conversely, sampling according to module (representing different interaction types or taxa) results in a rather complete view of certain modules, but fails to provide a complete picture of the underlying network. To reduce biases introduced by sampling methods, we recommend that these findings be incorporated into field design considerations for projects aiming to characterize large species interaction networks.

PEERJ 7, e7566, 2019. DOI: 10.7717/peerj.7566

[P352-2019] "Revisiting the fragile-to-strong crossover in metallic glass-forming liquids: Application to CuxZrxAl100-2x alloy"

Donado, R. A.*; Cajahuaringa, S.*; Antonelli, A.*

The fragile-to-strong crossover seems to be a general feature of metallic glass-forming liquids. Here, we study the behavior of shear viscosity, diffusion coefficient, and vibrational density of states for CuxZrxAl100-2x, alloy through molecular dynamics simulations. The results reveal that the fragile-to-strong temperature (T-fs) and the glass transition temperature (T-g) increase as the aluminum content becomes larger. The inverse of the diffusion coefficient as a function of temperature exhibits a dynamical crossover in the vicinity of T-g, at a much lower temperature than that predicted by nearly all previous studies. At the temperature in which the dynamical crossover occurs determined by the inverse of the diffusion coefficient, we found an excess of vibrational states at low frequencies, resembling a pronounced peak in the reduced vibrational density of states characteristic of a strong liquid.

Finally, the behavior of the shear viscosity as a function of reduced temperature (T-g/T) also shows that, aside from the fragile-to-strong crossover nearby T-g, another dynamical crossover is present near the onset of the supercooled regime.

PHYSICAL REVIEW MATERIALS 3[8], 085601, 2019. DOI: 10.1103/PhysRevMaterials.3.085601

[P353-2019] "Ringing revivals produced by non classical fields generated by conditional measurements"

Anaya-Contreras, J. A.; Zuniga-Segundo, A.; Soto-Eguibar, F.; Arrizon, V.; **Vidiella-Barranco, A.***; Moya-Cessa, H. M.

We study single photon resonant transitions of a two level atom with a quantized electromagnetic field when conditional measurements take place, showing that squeezed states may be generated in the multiphoton processes that occur during evolution. We examine some field properties and show that the field not only acquires squeezing properties but also may gain or lose more than one photon. Furthermore, the squeezing properties of the generated field are put in evidence by making it to interact with a second two level atom and observing the ringing revivals characteristic of the squeezed fields.

OPTIK 185, 721-725, 2019. DOI: 10.1016/j.ijleo.2019.03.139

[P354-2019] "Scanning Tunneling Measurements in Membrane-Based Nanostructures: Spatially-Resolved Quantum State Analysis in Postprocessed Epitaxial Systems for Optoelectronic Applications"

Rosa, B. L. T.; Parra-Murillo, C. A.; Chagas, T.; Garcia Junior, A. J.; Guimaraes, P. S. S.; **Deneke, C.***; Magalhaes-Paniago, R.; Malachias, A.

Nanoscale heterostructure engineering is the main target for the development of optoelectronic devices. In this sense, a precise knowledge of local electronic response after materials processing is required to envisage technological applications. A number of local probe techniques that address single nanostructure signals were satisfactorily employed in semiconductor epitaxial systems. In this work we show that the use of chemically etched semiconductor nanomembranes allows carrying out scanning tunneling spectroscopy (STS) measurements in a postprocessed system which was otherwise studied mainly under in situ conditions that differ from the operational regime. We were able to acquire STS spectra with energy level resolved response on InAs quantum dots grown within a 15 nm-thick GaAs single-crystalline film transferred to an Au(111) surface. The presence of a native oxide layer does not affect the result, keeping the reliability of the usual ultra high vacuum (UHV) procedures. The use of nanomembranes also opens up the possibility of tailoring properties via additional variables such as nanomembrane thickness and surface charge depletion. Our method is applicable to a broad class of postprocessed layers extracted in nanomembrane format from epitaxial systems that are potential candidates for optoelectronic applications.

ACS APPLIED NANO MATERIALS 2[7], 4655-4664, 2019. DOI: 10.1021/acsanm.9b01124

[P355-2019] "Search for an exotic decay of the Higgs boson to a pair of light pseudoscalars in the final state with two muons and two b quarks in pp collisions at 13 TeV"

Sirunyan, A. M.; Tumasyan, A.; Adam, W.; **Chinellato, J. A.*; Tonelli Manganote, E. J.***; et. al.; CMS Collaboration

A search for exotic decays of the Higgs boson to a pair of light pseudoscalar particles a(1) is performed under the hypothesis that one of the pseudoscalars decays to a pair of opposite sign muons and the other decays to b (b) over bar. Such signatures are predicted in a number of extensions of the standard model (SM), including next-to-minimal supersymmetry and two-Higgs-doublet models with an additional scalar singlet. The results are based on a data set of proton-proton collisions corresponding to an integrated luminosity of 35.9 fb(-1), accumulated with the CMS experiment at the CERN LHC in 2016 at a centre-of-mass energy of 13 TeV. No statistically significant excess is observed with respect to the SM backgrounds in the search region for pseudoscalar masses from 20 GeV to half of the Higgs boson mass. Upper limits at 95% confidence level are set on the product of the production cross section and branching fraction, sigma B-h(h -> a(1)a(1) -> mu (+)mu(-) b (b) over bar), ranging from 5 to 33 fb, depending on the pseudoscalar mass. Corresponding limits on the branching fraction, assuming the SM prediction for sigma(h), are (1-7) x 10(-4).

PHYSICS LETTERS B 795, 398-423, 2019. DOI: 10.1016/j.physletb.2019.06.021

[P356-2019] "Search for charged Higgs bosons in the H-+/- -> tau(+/-)nu(tau) decay channel in proton-proton collisions at s=13 TeV"

Sirunyan, A. M.; Tumasyan, A.; Adam, W.; **Chinellato, J. A.*; Tonelli Manganote, E. J.***; et. al.; CMS Collaboration

A search is presented for charged Higgs bosons in the H-+/- -> tau(+/-)nu(tau) decay mode in the hadronic final state and in final states with an electron or a muon. The search is based on proton-proton collision data recorded by the CMS experiment in 2016 at a center-of-mass energy of 13 TeV, corresponding to an integrated luminosity of 35.9 fb(-1). The results agree with the background expectation from the standard model. Upper limits at 95% confidence level are set on the production cross section times branching fraction to tau(+/-)nu(tau) for an H-+/- in the mass range of 80GeV to 3TeV, including the region near the top quark mass. The observed limit ranges from 6 pb at 80 GeV to 5 fb at 3 TeV. The limits are interpreted in the context of the minimal supersymmetric standard model m(h)(mod-) scenario.

JOURNAL OF HIGH ENERGY PHYSICS 7, 142, 2019. DOI: 10.1007/JHEP07(2019)142

[P357-2019] "Search for dark matter in events with a leptoquark and missing transverse momentum in proton-proton collisions at 13 TeV"

Sirunyan, A. M.; Tumasyan, A.; Adam, W.; **Chinellato, J. A.*; Tonelli Manganote, E. J.***; et. al.; CMS Collaboration

A search is presented for dark matter in proton-proton collisions at a center-of-mass energy of root s= 13 TeV using events with at least one high transverse momentum (p(T)) muon, at least one high-p(T) jet, and large missing transverse momentum. The data were collected with the CMS detector at the CERN LHC in 2016 and 2017, and correspond to an integrated luminosity of 77.4 fb(-1). In the examined scenario, a pair of scalar leptoquarks is assumed to be produced. One leptoquark decays to a muon and a jet while the other decays to dark matter and low-p(T) standard model particles. The signature for signal events would be significant missing transverse momentum from the dark matter in conjunction with a peak at the leptoquark mass in the invariant mass distribution of the highest p(T) muon and jet. The data are observed to be consistent with the background predicted by the standard model.

For the first benchmark scenario considered, dark matter masses up to 500 GeV are excluded for leptoquark masses m(LQ) approximate to 1400 GeV, and up to 300 GeV for m(LQ) approximate to 1500 GeV. For the second benchmark scenario, dark matter masses up to 600 GeV are excluded for m(LQ) approximate to 1400 GeV.

PHYSICS LETTERS B 795, 76-99, 2019. DOI: 10.1016/j.physletb.2019.05.046

[P358-2019] "Search for supersymmetry with a compressed mass spectrum in the vector boson fusion topology with 1-lepton and 0-lepton final states in proton-proton collisions at p root s=13 TeV"

Sirunyan, A. M.; Tumasyan, A.; Adam, W.; **Chinellato, J. A.*; Tonelli Manganote, E. J.***; et. al.; CMS Collaboration

A search for supersymmetric particles produced in the vector boson fusion topology in proton-proton collisions is presented. The search targets final states with one or zero leptons, large missing transverse momentum, and two jets with a large separation in rapidity. The data sample corresponds to an integrated luminosity of 35.9 fb(-1) of proton-proton collisions at root s = 13TeV collected in 2016 with the CMS detector at the LHC. The observed dijet invariant mass and lepton-neutrino transverse mass spectra are found to be consistent with the standard model predictions. Upper limits are set on the cross sections for chargino ((chi) over tilde (+/-)(1)) and neutralino ((chi) over tilde (0)(2)) production with two associated jets. For a compressed mass spectrum scenario in which the (chi) over tilde (+/-)(1) and (chi) over tilde (0)(2) decays proceed via a light slepton and the mass difference between the lightest neutralino chi(0)(1) and the mass-degenerate particles (chi) over tilde (+/-)(1) and (chi) over tilde (0)(2) is 1 (30) GeV, the most stringent lower limit to date of 112 (215) GeV is set on the mass of these latter two particles.

JOURNAL OF HIGH ENERGY PHYSICS 8, 150, 2019. DOI: 10.1007/JHEP08(2019)150

[P359-2019] "Search for the production of (WWW -/+)-W--+/--W-+/- events at root s=13 TeV"

Sirunyan, A. M.; Tumasyan, A.; Adam, W.; **Chinellato, J. A.*; Tonelli Manganote, E. J.***; et. al.; CMS Collaboration

A search for the production of events containing three W bosons predicted by the standard model is reported. The search is based on a data sample of proton-proton collisions at a center--of-mass energy of 13 TeV recorded by the CMS experiment at the CERN LHC and corresponding to a total integrated luminosity of 35.9 fb(-1). The search is performed in final states with three leptons (electrons or muons), or with two same-charge leptons plus two jets. The observed (expected) significance of the signal for (WWW -/+)-W-+/--W-+/- production is 0.60 (1.78) standard deviations, and the ratio of the measured signal yield to that expected from the standard model is 0.34(-0.34) (+0.62) . Limits are placed on three anomalous quartic gauge couplings and on the production of massive axionlike particles.

PHYSICAL REVIEW D 100[1], 012004, 2019. DOI: 10.1103/PhysRevD.100.012004

[P360-2019] "Search for vectorlike leptons in multilepton final states in proton-proton collisions at root s=13 TeV"

Sirunyan, A. M.; Tumasyan, A.; Adam, W.; **Chinellato, J. A.*; Tonelli Manganote, E. J.***; et. al.; CMS Collaboration

A search for vectorlike leptons in multilepton final states is presented. The data sample corresponds to an integrated luminosity of 77.4 fb(-1) of proton-proton collisions at a center-of--mass energy of 13 TeV collected by the CMS experiment at the LHC in 2016 and 2017. Events are categorized by the multiplicity of electrons, muons, and hadronically decaying tau leptons. The missing transverse momentum and the scalar sum of the lepton transverse momenta are used to distinguish the signal from background. The observed results are consistent with the expectations from the standard model hypothesis. The existence of a vectorlike lepton doublet, coupling to the third-generation standard model leptons in the mass range of 120-790 GeV, is excluded at 95% confidence level. These are the most stringent limits yet on the production of a vectorlike lepton doublet, coupling to the third-generation standard model leptons.

PHYSICAL REVIEW D 100[5], 052003, 2019. DOI: 10.1103/PhysRevD.100.052003

[P361-2019] "Segmentation of nearly isotropic overlapped tracks in photomicrographs using successive erosions as watershed markers"

de Siqueira, A. F.*; Nakasuga, W. M.*; Guedes, S.*; Ratschbacher, L.

Introduction Procedures for measuring and counting tracks are time-consuming and involve practical problems. The precision of automatic counting methods is not satisfactory yet; the major challenges are distinguishing tracks and material defects, identifying small tracks and defects of similar size, and detecting overlapping tracks. Materials and Methods Here, we address the overlapping tracks issue using the algorithm Watershed Using Successive Erosions as Markers (WUSEM), which combines the watershed transform, morphological erosions and labeling to separate regions in photomicrographs. We tested this method in two data sets of diallyl phthalate (DAP) photomicrographs and compared the results when counting manually and using the classic watershed and H-watershed transforms. Results The mean automatic/manual efficiency counting ratio when using WUSEM in the test data sets is 0.97 +/- 0.11. Conclusion WUSEM shows reliable results when used in photomicrographs presenting almost isotropic objects. Also, diameter and eccentricity criteria may be used to increase the reliability of this method.

MICROSCOPY RESEARCH AND TECHNIQUE 82[10], 1706-1719, 2019. DOI: 10.1002/jemt.23336

[P362-2019] "Solid-liquid phase equilibrium diagrams of binary mixtures containing fatty acids, fatty alcohol compounds and tripalmitin using differential scanning calorimetry"

Pelaquim, F. P.; Matos, F. C. de; **Cardoso, L. P.***; Batista, E. A. C.; Meirelles, A. J. de A.; da Costa, M. C.

Fatty acids, fatty alcohol compounds and triacylglycerols (TAGs) present a significant role in industrial applications, mainly in food, cosmetics and pharmaceutical industries. In this study, eight solid-liquid phase diagrams composed by tripalmitin plus fatty acids (capric acid, lauric acid, myristic acid, palmitic acid and stearic acid) and tripalmitin plus fatty alcohol compounds (1-decanol, 1-dodecanol and 1-tetradecanol) were studied using Differential Scanning Calorimetry (DSC) technique, optical microscopy and X-ray analysis. The phase diagrams formed by tripalmitin + fatty acids (myristic acid, palmitic acid and stearic acid), present a eutectic behavior with a solid solution for tripalmitin (1) + myristic acid (4) system, and a monotectic behavior for tripalmitin + (capric acid and lauric acid) whereas the phase diagrams formed by tripalmitin + fatty alcohol compounds present a monotectic behavior and just one of them present a monotectic behavior with a solid solution (1-tetradecanol).

The liquid phase was modelled using ideal assumption, 3-suffix Margules and NRTL models, adjusting its parameters. These models described properly the liquidus line of the systems studied.

FLUID PHASE EQUILIBRIA 497, 19-32, 2019. DOI: 10.1016/j.fluid.2019.05.020

[P363-2019] "Space-time recurrences for functional connectivity evaluation and feature extraction in motor imagery brain-computer interfaces"

Rodrigues, P. G.; **Stefano Filho, C. A.***; Attux, R.; **Castellano, G.***; Soriano, D. C.

This work presents a classification performance comparison between different frameworks for functional connectivity evaluation and complex network feature extraction aiming to distinguish motor imagery classes in electroencephalography (EEG)-based brain-computer interfaces (BCIs). The analysis was performed in two online datasets: (1) a classical benchmark-the BCI competition IV dataset 2a-allowing a comparison with a representative set of strategies previously employed in this BCI paradigm and (2) a statistically representative dataset for signal processing technique comparisons over 52 subjects. Besides exploring three classical similarity measures-Pearson correlation, Spearman correlation, and mean phase coherence-this work also proposes a recurrence-based alternative for estimating EEG brain functional connectivity, which takes into account the recurrence density between pairwise electrodes over a time window. These strategies were followed by graph feature evaluation considering clustering coefficient, degree, betweenness centrality, and eigenvector centrality. The features were selected by Fisher's discriminating ratio and classification was performed by a least squares classifier in agreement with classical and online BCI processing strategies. The results revealed that the recurrence-based approach for functional connectivity evaluation was significantly better than the other frameworks, which is probably associated with the use of higher order statistics underlying the electrode joint probability estimation and a higher capability of capturing nonlinear inter-relations. There were no significant differences in performance among the evaluated graph features, but the eigenvector centrality was the best feature regarding processing time. Finally, the best ranked graph-based attributes were found in classical EEG motor cortex positions for the subjects with best performances, relating functional organization and motor activity.

MEDICAL & BIOLOGICAL ENGINEERING & COMPUTING 57[8], 1709-1725, 2019. DOI: 10.1007/s11517-019-01989-w

[P364-2019] "Statistical thermodynamics of the Frohlich--Bose-Einstein condensation of magnons out of equilibrium"

Vannucchi, F. S.; **Luzzi, R.***

This work presents a nonequilibrium statistical-thermodynamic approach to the study of a Frohlich-Bose-Einstein condensation of magnons under radio-frequency radiation pumping. Frohlich-Bose-Einstein condensates display a complex behavior consisting in steady-state conditions to the emergence of a synergetic dissipative structure resembling the Bose-Einstein condensation of systems in equilibrium. Then a kind of "two-fluid model" arises: the "normal" nonequilibrium structure and the Frohlich condensate, which is shown to be an attractor to the system. In this study we analyze some aspects of the irreversible thermodynamics of this dissipative complex system. We obtained the expression for the informational entropy of the two-fluid condensate and introduced an order parameter to characterize the role of the Frohlich interaction in ordering the system. The analysis highlights the order increase due to the Frohlich interaction. We also study the informational entropy production of the system, considering its internal and external parts. Finally, the Glansdorff-Prigogine criteria for evolution and (in) stability are verified.

PHYSICAL REVIEW E 100[3], 032126, 2019. DOI: 10.1103/PhysRevE.100.032126

[P365-2019] "Structural Analysis of Ligand-Protected Smaller Metallic Nanocrystals by Atomic Pair Distribution Function under Precession Electron Diffraction"

Hoque, M. M.; Vergara, S.; Das, P. P.; **Ugarte, D.***; Santiago, U.; Kumara, C.; Whetten, R. L.; Dass, A.; Ponce, A.

Atomic pair distribution function (PDF) analysis has been widely used to investigate nanocrystalline and structurally disordered materials. Experimental PDFs retrieved from electron diffraction (ePDF) in transmission electron microscopy (TEM) represent an attractive alternative to traditional PDF obtained from synchrotron X-ray sources, particularly for studying minute samples. Nonetheless, the inelastic scattering produced by the large dynamical effects of electron diffraction may obscure the interpretation of ePDF. In the present work, precession electron diffraction (PED-TEM) has been employed to obtain the ePDF of two different samples-lipoic acid- and hexanethiolate-capped gold nanoparticles (similar to 4.5 and 4.2 nm, respectively) randomly oriented and measured at both liquid nitrogen and room temperatures. The electron diffraction data were processed to obtain ePDFs which were subsequently compared with the PDF of different ideal structure models. The results demonstrate that the PED-ePDF data are sensitive to different crystalline structures such as monocrystalline (truncated octahedra) and multiply twinned (decahedra, icosahedra) structures. The results indicate that PED reduces the residual from 46 to 29%; in addition, the combination of PED and low temperature further reduced the residual to 23%, which is comparable to X-ray PDF analysis. Furthermore, the inclusion of PED resulted in a better estimation of the coordination number from ePDF. To the best of our knowledge, the precessed electron-beam technique (PED) has not been previously applied to nanoparticles for analysis by the ePDF method.

JOURNAL OF PHYSICAL CHEMISTRY C 123[32], 19894-19902, 2019. DOI: 10.1021/acs.jpcc.9b02901 **(Artigo destaque de capa)**

[P366-2019] "The Morphology and Structure of Stellar Populations in the Fornax Dwarf Spheroidal Galaxy from Dark Energy Survey Data"

Wang, M. Y.; de Boer, T.; Pieres, A.; **Sobreira, F.***; et. al.; DES Collaboration

Using deep wide-field photometry 3 yr data (Y3) from the Dark Energy Survey (DES), we present a panoramic study of the Fornax dwarf spheroidal galaxy. The data presented here-a small subset of the full survey-uniformly cover a region of 25 deg(2) centered on the galaxy to a depth of g similar to 23.5. We use these data to study the structural properties of Fornax, overall stellar population, and its member stars in different evolutionary phases. We also search for possible signs of tidal disturbance. Fornax is found to be significantly more spatially extended than what early studies suggested. No statistically significant distortions or signs of tidal disturbances were found down to a surface brightness limit of similar to 32.1 mag arcsec(-2). However, there are hints of shell-like features located similar to 20'-40' from the center of Fornax that may be stellar debris from past merger events. We also find that intermediate-age and young main-sequence populations show different orientation at the galaxy center and have many substructures.

The deep DES Y3 data allow us to characterize the age of those young stellar substructures with great accuracy, both those previously known and those newly identified as possible overdensities in this work, on the basis of their color-magnitude diagram morphology. We find that the youngest overdensities are all found on the eastern side of Fornax, where the Fornax field population itself is slightly younger than in the west. In summary, the high-quality DES Y3 data reveal that Fornax has many rich structures and provide insights into its complex formation history.

ASTROPHYSICAL JOURNAL 881[2], 118, 2019. DOI: 10.3847/1538-4357/ab31a9

[P367-2019] "THE POTENTIAL OF STRUCTURED NARRATIVES FOR COMPUTATIONAL JOURNALISM: JOURNALISTIC SKILLS IN THE ELABORATION OF DATABASE GENERATED TEXTS"

Azzellini, E. C.; Peschanski, J. A.; **da Paixao, F. J.***

In this article, we explore the digital skills developed by journalists in the informational context of Big Data that raise the feasibility of intersection between Computer Science and Journalism. In this sense, authors propose different understandings of the Computational Journalism, a hypothetical field in which the journalistic practice adds a technical direction, which expands the horizon of understanding of the relation of the journalist to the narrative construction in the environment of abundance of data. In this scenario we observe the emergence of experiments with structured narratives, understood as verbal texts automated from predetermined templates that process data from structured databases. With this, the article reflects on Natural Language Generation (NLG) software in news composition and presents results of the development of the Mbabel tool for generating structured drafts for thematic entries in Wikipedia from the Wikidata database.

TEXTO LIVRE-LINGUAGEM E TECNOLOGIA 12[1], 138-152, 2019. DOI: 10.17851/1983-3652.12.1.138-152

[P368-2019] "The Thermomechanical Properties of Thermally Evaporated Bismuth Triiodide Thin Films"

Coutinho, N. F.*; Cucatti, S.*; Merlo, R. B.*; Silva Filho, J. M. C.*; Villegas, N. F. B.*; Alvarez, F.*; Nogueira, A. F.; **Marques, F. C.***

Bismuth triiodide (BiI3) has been studied in recent years with the aim of developing lead-free semiconductors for photovoltaics. It has also appeared in X-ray detectors due to the high density of the Bismuth element. This material is attractive as an active layer in solar cells, or may be feasible for conversion into perovskite-like material (MA(3)Bi(2)I(9)), being also suitable for photovoltaic applications. In this study, we report on the thermomechanical properties (stress, hardness, coefficient of thermal expansion, and biaxial and reduced Young's moduli) of BiI3 thin films deposited by thermal evaporation. The stress was determined as a function of temperature, adopting the thermally induced bending technique, which allowed us to extract the coefficient of thermal expansion (31 x 10(-6) degrees C-1) and Young's biaxial modulus (19.6 GPa) for the films. Nanohardness (similar to 0.76 GPa) and a reduced Young's modulus of 27.1 GPa were determined through nanoindentation measurements.

SCIENTIFIC REPORTS 9, 11785, 2019. DOI: 10.1038/s41598-019-48194-1

[P369-2019] "Torsional oscillations of magnetized neutron stars with mixed poloidal-toroidal fields"

de Souza, G. H.*; Chirenti, C.

The quasiperiodic oscillations found in the three giant flares of soft gamma-ray repeaters observed to date have been interpreted as torsional oscillations caused by a starquake related to a magnetospheric reconnection event. Motivated by these observations, we study the influence of the magnetic field geometry in the frequencies of the torsional oscillations of magnetized neutron stars. We use realistic tabulated equations of state for the core and crust of the stars and model their magnetic field as a dipole plus a toroidal component, using the relativistic Grad-Shafranov equation. The frequencies of the torsional modes are obtained by the numerical solution of the eigenvalue problem posed by the linear perturbation equations in the Cowling approximation. Our results show how the asteroseismology of these stars becomes complicated by the degeneracy in the frequencies due to the large relevant parameter space. However, we are able to propose approximately equation-of-state-independent relations that parametrize the influence of the magnetic field in the torsional oscillations, as well as a testable scenario in which the rearrangement of the magnetic field causes an evolution of the frequencies. Finally, we show that there is a magnetic field configuration that maximizes the energy in the perturbation at linear order, which could be related to the trigger of the giant flare.

PHYSICAL REVIEW D 100[4], 043017, 2019. DOI: 10.1103/PhysRevD.100.043017

[P370-2019] "Transcription regulators are transiently expressed during the prostate gland adaptation to the hypoandrogenic environment"

Nishan, U.; Rosa-Ribeiro, R.; **Cesar, C. L.***; Carvalho, H. F.

The high incidence of prostatic diseases, including malignant tumors, makes the understanding of prostate biology very important. Androgen deprivation, blockade by orchiectomy, or chemical castration causes prostate and tumor shrinkage. The gene networks involved in a cell type-specific fashion are rather unknown. This work was undertaken to identify genes with annotated function in transcription regulation that might define transitions in gene expression. A total of 15 potential regulatory genes were identified. Validation by qRT-PCR showed that Zfp703 and Arid1a exhibit expression maxima at day 1; Ash2l, Nelf, Pbx3, Eya2 at day 4; Dmrt2 at day 5 and Lbh and Sox1 at day 7 after castration. Using immunohistochemistry, we further determined that PBX3 was found in both stromal and epithelial cells, whereas ARID1A and NELF were restricted to the epithelium, and DMRT2 and EYA2 were exclusively found in the stroma. Though the proteins ZFP703 and ASH2l were not found in any experimental condition, their mRNAs were located by in situ hybridization in both epithelium and stroma. In conclusion, androgen deprivation triggers the expression of temporally regulated gene sets in both epithelial and stromal cells. These gene subsets will help establish the regulatory gene expression programs orchestrating the castration-induced remodeling of the prostate gland, and represent putative targets to increase the efficacy of androgen-deprivation to induce epithelial (and cancer) cell death.

HISTOLOGY AND HISTOPATHOLOGY 34[9], 1025-1036, 2019. DOI: 10.14670/HH-18-105

[P371-2019] "Tuning high power impulse magnetron sputtering discharge and substrate bias conditions to reduce the intrinsic stress of TiN thin films"

Cemin, F.*; Abadias, G.; Minea, T.; Lundin, D.

Ion bombardment during film growth usually induces high compressive stress in compound thin film materials, resulting in rupture and failure of coated tools used in tribological applications.

Hence, intrinsic stress generated during film growth can drastically limit the industrial appeal of deposition technologies such as high power impulse magnetron sputtering (HiPIMS). This work investigates how to reduce high stress levels by tuning the HiPIMS discharge conditions and selecting the appropriate substrate bias configuration. The strategy is based on optimizing the process discharge parameters, leading to HiPIMS discharges containing fewer multiply charged energetic metal ions, which is combined with pulsed substrate bias synchronized to the HiPIMS pulse to control the chemical nature of the incident ions, i.e., inert gas vs. metal ions. The study was performed during growth of TiN thin films, due to their relevance as a protective coating, and the intrinsic stress was measured in situ during film growth using the wafer curvature method and a multi-beam optical stress sensor. The results show that for standard HiPIMS discharges and biased substrates, the energetic metal ion bombardment results in very dense, compact microstructures, but highly stressed TiN films. On the other hand, when using the here proposed strategy mentioned above, the compressive stress was considerably reduced (by a factor 11) while retaining rather compact microstructures compared to direct current magnetron sputtered as well as non-biased HiPIMS samples.

THIN SOLID FILMS 688[SI}, UNSP 137335, 2019. DOI: 10.1016/j.tsf.2019.05.054

[P372-2019] "Ultra-thin films of In on Pd(111) characterized by X-ray photoelectron diffraction"

Pancotti, A.; **de Siervo, A.***; Carazzolle, M. F.; **Landers, R.***; Nascente, P. A. P.

Metallic surfaces involving transition metals are widely used in the preparation of catalysts. The conversion rates and the selectivity can be improved, in many instances, by a surface alloy formed by a transition metal with a less reactive sp metal. Bimetallic systems based on Pd-In have been shown to be efficient catalysts for methanol steam reforming and nitrate reduction in water. The catalytic reaction depends on both the electronic structure and the geometric arrangement of the surface alloy atoms. In and Pd have very limited miscibility in the bulk but can form ordered surface alloys. We have investigated the growth and the surface alloy formation of an ultra-thin film of In deposited on a Pd(111) single-crystal substrate surface. The electronic structure and the surface composition have been characterized by X-ray photoelectron spectroscopy (XPS), and the atomic surface structure has been determined by a combination of low energy electron diffraction (LEED) and X-ray photoelectron diffraction (XPD). Ultra-thin films of In having approximately 1 to 5 monolayers (ML) were deposited at room temperature, and then annealed at 500 K. Pd 3d and In 3d intensities obtained by XPS indicated the Stranski-Krastanov growth mode, i.e. flat bi-dimensional overlayers in the first layer followed by three-dimensional islands. For annealed In films having 0.33 to 2.5 ML, a (root 3x root 3) R30 degrees LEED pattern was observed. For a non-annealed In film having approximately 3 ML, a p(2 x 2) LEED pattern was observed, that changed to (root 3x root 3)R30 degrees upon annealing at 500 K. For a slightly higher coverage, about 3.6 ML, a (1 x 1) pattern was obtained after annealing. XPS results for the annealed similar to 3.6 ML film indicate the diffusion of In atoms into the outermost layers of the Pd(111) single-crystal. For the same In film, XPD indicated the formation of bi-dimensional In islands, with some bare patches of the substrate.

THIN SOLID FILMS 688[SI], UNSP 137442, 2019. DOI: 10.1016/j.tsf.2019.137442

[P373-2019] "Unconventional spin-glass-like state in AgCo2V3O10, the novel magnetically frustrated material"

Hadouchi, M.; Assani, A.; Saadi, M.; **Kopelevich, Y.*; da Silva, R. R.***; Lahmar, A.; Bouyanfif, H.; El Marssi, M.; El Ammari, L.

Single crystals of a new silver and-cobalt based vanadate AgCo2V3O10 were grown from a melted mixture. The crystal structure determination reveals that this new vanadate crystallizes in triclinic system with space group P (1) over bar. The structure of the filed compound is constructed from CoO6 octahedra and VO4 tetrahedra sharing edges and vertices leading to an open three-dimensional framework delimiting tunnels along [0 0 1], where the Ag cations are located. The bands observed in Raman spectrum were assigned to corresponding vibrations of the VO4 groups. DC and AC magnetization (susceptibility) measurements revealed the spin-glass (SG) - type transition below a frequency-dependent temperature T-f(H) that is nearly independent on the applied magnetic field. Magnetic field H > 10 kOe induces the spin glass--antiferromagnet. These observations brings AgCo2 V3O10 into the class of geometrically frustrated magnetic systems.

JOURNAL OF MAGNETISM AND MAGNETIC MATERIALS 491, UNSP 165623, 2019. DOI: 10.1016/j.jmmm.2019.165623

[P374-2019] "Zero-field-cooled exchange bias effect in phase-segregated La2-xA(x)CoMnO(6-delta) (A = Ba,Ca,Sr; x=0, 0.5)"

Coutrim, L. T.; **Rigitano, D.***; Macchiutti, C.; Mori, T. J. A.; Lora-Serrano, R.; **Granado, E.***; Sadrollahi, E.; Litterst, F. J.; Fontes, M. B.; Baggio-Saitovitch, E.; Bittar, E. M.; Bufaical, L.

In the zero-field-cooled exchange bias (ZEB) effect, the unidirectional magnetic anisotropy is set at low temperatures even when the system is cooled in the absence of an external magnetic field. La1.5Sr0.5CoMnO6 stands out as presenting the largest ZEB reported so far, while for La1.5Ca0.5CoMnO6 the exchange bias field (HEB) is one order of magnitude smaller. Here we show that La1.5Ba0.5CoMnO6 also exhibits a pronounced shift of its magnetic hysteresis loop, with an intermediate H-EB value with respect to Ca- and Sr-doped samples. To figure out the microscopic mechanisms responsible for this phenomenon, these compounds were investigated by means of synchrotron x-ray powder diffraction, Raman spectroscopy, muon spin rotation and relaxation, ac and dc magnetization, x-ray absorption spectroscopy (XAS), and x-ray magnetic circular dichroism (XMCD). The parent compound La2CoMnO6 was also studied for comparison as a reference of a non-ZEB material. Our results show that the Ba-, Ca-, and Sr-doped samples present a small amount of phase segregation, and that the ZEB effect is strongly correlated to the system's structure. We also observed that mixed valence states Co2+/Co3+ and Mn4+/Mn3+ are already present at the La2CoMnO6 parent compound, and that Ba2+/Ca2+/Sr2+ partial substitution at the La3+ site leads to a large increase of Co average valence, with a subtle augmentation of Mn formal valence. Estimates of the Co and Mn valences from the L-edge XAS indicate the presence of oxygen vacancies in all samples (0.05 <= delta <= 0.1). Our XMCD results show a great decrease of Co moment for the doped compounds, and they indicate that the shift of the hysteresis curves for these samples is related to uncompensated antiferromagnetic coupling between Co and Mn.

PHYSICAL REVIEW B 100[5], 054428, 2019. DOI: 10.1103/PhysRevB.100.054428

Eventos publicados

[P375-2019] "Comparative study between wet and dry etching of silicon for microchannels fabrication"

Cirino, G. A.; Barea, L. A. M.; Mansano, R. D.; Verdonck, P.; **von Zuben, A.***; Frateschi, N. C.*; Diniz, J. A.

In this work we present a comparative study of two processes for the fabrication of an array of microchannels for microfluidics applications, based on integrated-circuit technology process steps, such as lithography and dry etching. Two different methods were investigated in order to study the resulting microstructures: wet and dry deep etching of silicon substrate. The typical etching depth necessary to the target application is 50 mu m.

Conference on Advanced Fabrication Technologies for Micro/Nano Optics and Photonics XII; FEB 03-05, 2019 San Francisco, CA
ADVANCED FABRICATION TECHNOLOGIES FOR MICRO/NANO OPTICS AND PHOTONICS XII Proceedings of SPIE 10930, 1093015, 2019. DOI: 10.1117/12.2506804

[P376-2019] "Embedded-core optical fiber for distributed pressure measurement using an autocorrelation OFDR technique"

Gerosa, R. M.; **Osorio, J. H.***; Lopez-Cortes, D.; **Cordeiro, C. M. B.***; de Matos, C. J. S.

We present a pressure sensor using an optical frequency domain reflectometer and a simplified microstructured fiber. High sensitivity, ease of fabrication and distributed sensing makes the proposed configuration a promising technique for pressure sensing applications.

Conference on Lasers and Electro-Optics (CLEO) MAY 05-10, 2019 San Jose, CA

[P377-2019] "Polarization-Selective Excitation of Triplet State Coherences in CsPbI3 Perovskite Nanocrystals"

Liu, A.; Almeidal, D. B.; Bonato, L. G.; **Nagamine, G.*; Zagonel, L. F.***; Nogueira, A. F.; **Padilha, L. A.***; Cundiffl, S. T.

We study CsPbI3 perovskite nanocrystals using polarization--resolved 2D coherent spectroscopy at cryogenic temperatures. Coherences involving triplet exciton states are revealed and characterized, including inter-triplet coherences with dephasing times on the picosecond timescale.

Conference on Lasers and Electro-Optics (CLEO) MAY 05-10, 2019 San Jose, CA

[P378-2019] "Tunable III-V-on-Si Laser with Resonant Photonic Molecule Mirrors"

Rezende, G. F. M. de*; Frateschi, N. C.*; Roelkens, G.

We propose, fabricate and characterize a novel III-V-on--Si laser. Resonant mirrors are realized by tailoring supermodes of coupled microrings. A threshold of 40mA, series resistance of 10 Omega and SMSR of 40dB is reported.

Conference on Lasers and Electro-Optics (CLEO) MAY 05-10, 2019 San Jose, CA

Artigos aceitos para publicação

[A002-2019] "The structure of graphene on graphene/C60/Cu interfaces: a molecular dynamics study"

Fonseca, A. F.*; Dantas, S.*; Galvão, D. S.*; Zhang, D.; Sinnott, S. B.

Two experimental studies reported the spontaneous formation of amorphous and crystalline structures of C60 molecules intercalated between graphene and a surface. The findings observed included interesting phenomena ranging from reaction between fullerene C60s ('C60s' stands for plural of C60) under graphene to graphene sheets sagging between C60s and control of strain in these sheets. Motivated by this work, we performed fully atomistic reactive molecular dynamics simulations to investigate the formation and thermal stability of graphene sheet wrinkles as well as graphene attachment to and detachment from a surface when the sheet is laid over a previously distributed array of C60 molecules on a copper surface at different temperatures. As graphene compresses the C60s against the surface, and graphene attachment to the surface in between C60s depends on the height of the wrinkles in the graphene sheet, configurations with both frozen and non-frozen fullerenes were investigated in the simulations in order to examine the experimental result of stable, sagged graphene sheets when the distance between C60s is about 4 nm and the height of the wrinkles in the sheet is about 0.8 nm. Below a distance of 4 nm between fullerenes, the graphene is predicted to become locally suspended and less strained. The simulations predict that this happens when the fullerenes can deform under the compressive action of the graphene sheet. If the fullerenes are kept frozen, spontaneous 'blanketing' of graphene is predicted only when the distance between neighbouring C60s is equal to or great than about 7 nm. These predictions agree with a mechanical model relating the rigidity of a graphene sheet to the energy of graphene-surface adhesion. This work further reveals the structure of intercalated molecules and the role of stability and sheet wrinkling on the preferred configuration of graphene. This study thus might assist in the development of two-dimensional confined nanoreactors for chemical reactions.

NANOTECHNOLOGY 30, 505707, 2019. DOI: 10.1088/1361-6528/ab4431

[A003-2019] "Torsional refrigeration by twisted, coiled, and supercoiled fibers"

Wang, R.; Fang, S.; Xiao, Y.; Gao, E.; Jiang, N.; Li, Y.; Mou, L.; Shen, Y.; Zhao, W.; Li, S.; **Fonseca, A. F.*; Galvão, D. S.*;** Chen, M.; He, W.; Yu, K.; Lu, H.; Wang, X.; Qian, D.; Aliev, A. E.; Li, N.; Haines, C. S.; Liu, Z.; Mu, J.; Wang, Z.; Yin, S.; Lima, M. D.; An, B.; Zhou, X.; Liu, Z.; Baughman, R. H.

Higher-efficiency, lower-cost refrigeration is needed for both large- and small-scale cooling. Refrigerators using entropy changes during cycles of stretching or hydrostatic compression of a solid are possible alternatives to the vapor-compression fridges found in homes. We show that high cooling results from twist changes for twisted, coiled, or supercoiled fibers, including those of natural rubber, nickel titanium, and polyethylene fishing line. Using opposite chiralities of twist and coiling produces supercoiled natural rubber fibers and coiled fishing line fibers that cool when stretched. A demonstrated twist-based device for cooling flowing water provides high cooling energy and device efficiency. Mechanical calculations describe the axial and spring-index dependencies of twist-enhanced cooling and its origin in a phase transformation for polyethylene fibers.

SCIENCE 366[6462], 216-221, 2019. DOI: 10.1126/science.aax6182

***Autores da comunidade IFGW**
Fonte: Web of Science on-line (WOS)

Defesas de Teses do IFGW

[T008-2019] "Hádrons multi-estranhos em colisões Pb-Pb no LHC com o ALICE"
Aluno: Danilo Silva de Albuquerque
Orientador: Prof. Dr. Jun Takahashi
Data: 16/08/2019

[T009-2019] "Estudo da Influência de Substratos Nano-Estruturados por Bombardeamento Iônico no Crescimento e Organização de Partículas de Níquel"
Aluno: Mónica Morales Corredor
Orientador: Prof. Dr. Fernando Alvarez
Data: 10/09/2019

[T010-2019] "Fenômenos exóticos em sistemas de baixa dimensionalidade"
Aluno: Thaís Victa Trevisan
Orientador: Prof. Dr. Amir Ordacgi Caldeira
Data: 11/09/2019

[T011-2019] "Correções de derivadas superiores ao modelo inflacionário R+R2 e áxions no modelo 3-3-1"
Aluno: Ana Rubiela Romero Castellano
Orientador: Prof. Dr. Pedro Cunha de Holanda
Data: 18/09/2019

[T012-2019] "Transporte em cadeias de spin desordenadas"
Aluno: Luiz Filipe Campos Faria
Orientador: Prof. Dr. Eduardo Miranda
Data: 20/09/2019

[T013-2019] "Fenomenología do modelo SU(3)coSU(3) LoU(1)N"
Aluno: Carlos Enrique Alvarez Salazar
Orientador: Prof. Dr. Orlando Luis Goulart Peres
Data: 23/09/2019

[T014-2019] "Characterization and manipulation of optical modes in photonic crystal fibers"
Aluno: Erick Abraham Lamilla Rubio
Orientador: Prof. Dr. Paulo Clóvis Dainese Junior
Data: 25/09/2019

Defesas de Dissertações do IFGW

[D016-2019] "Crescimento de nanoestruturas de manganês em substrato monocristalino de cromo (100)"
Aluno: Lucas Capel Godinho
Orientador: Prof. Dr. Julio Criginski Cézar
Data: 26/09/2019

[D017-2019] "Emaranhamento entre Íons Aprisionados em uma Rede de Cavidades Acopladas sob Influência de Dissipações"
Aluno: Alessandro Silva Santana
Orientador: Prof. Dr. José Antonio Roversi
Data: 30/09/2019

[D018-2019] "Estudo in-situ da interação entre domínios ferroelétricos e ferromagnéticos de heteroestruturas de Fe e BaTiO3"
Aluno: Felipe Luiz Alvares Vital
Orientador: Prof. Dr. Julio Criginski Cezar
Data: 30/09/2019

[D019-2019] "A Física de Neutrinos no Formalismo de Matriz Densidade"
Aluno: Rafaela Rodrigues Rossi
Orientador: Prof. Dr. Orlando Luis Goulart Peres
Data: 03/10/2019

[D020-2019] "Quebra espontânea de simetria de rotação no composto CeRhIn(5)"
Aluno: Mário Malcolms de Oliveira
Orientador: Prof. Dr. Eduardo Miranda
Data: 07/10/2019

[D021-2019] "Desenho, fabricação e caracterização de dispositivos de guias de onda acoplados para medida da força de batimento"
Aluno: Cauê Moreno Kersul de Castro Carvalho
Orientador: Prof. Dr. Pierre-Louis de Assis
Data: 11/10/2019

Fonte: Portal IFGW/Pós-graduação - Agenda de Colóquios, Defesas e Seminários.
Disponível em: http://portal.ifi.unicamp.br/pos-graduacao

***Nestes meses não há Defesas de Dissertações e Teses do PECIM com Orientadores do IFGW.**

Em comemoração à Semana do Livro e da Biblioteca e a Semana Internacional de Acesso Aberto 2019, a Biblioteca “Prof. Marcello Damy” do Instituto de Física “Gleb “Wataghin” lança um FAQ sobre Acesso Aberto com o objetivo de reunir informações sobre o tema e ser, de alguma forma, um guia aos pesquisadores. A chamada Ciência Aberta traz consigo uma série de desafios, a questão do Acesso Aberto das publicações científicas é um deles. Nesse sentido e em consonância com esse Movimento Internacional de Acesso Aberto, esperamos que esse FAQ possa ser útil a você. Estar bem informado fará toda a diferença!

Acesse: https://portal.ifi.unicamp.br/biblioteca/acesso-aberto

Abstracta

Instituto de Física
Diretor: Prof. Dr. Pascoal José Giglio Pagliuso
Diretora Associada: Profa. Dra. Mônica Alonso Cotta
Universidade Estadual de Campinas - UNICAMP
Cidade Universitária Zeferino Vaz
13083-859 - Campinas - SP - Brasil
e-mail: secdir@ifi.unicamp.br
Fone: +55 19 3521-5300

Publicação

Biblioteca do Instituto de Física Gleb Wataghin
http://portal.ifi.unicamp.br/biblioteca

Diretora Técnica: Sandra Maria Carlos Cartaxo
Coordenadora da Comissão de Biblioteca: Profa. Dra. Arlene Cristina Aguilar

Elaboração:
Maria Graciele Trevisan (Bibliotecária)
Ayres Neri da Cunha Junior (Técnico Administrativo)
contato: infobif@ifi.unicamp.br